Improved constraints on transit time distributions from argon 39: A maximum entropy approach

Mark Holzer[1,2] and François W. Primeau[3]

[1]   We use ^{39}Ar in conjunction with CFCs, natural radiocarbon, and the cyclostationary tracers PO_4*, temperature, and salinity to estimate the ocean's transit time distributions (TTDs). A maximum entropy method is employed to deconvolve the tracer data for the TTDs. The constraint provided by the ^{39}Ar data allows us to estimate TTDs even in the deep Pacific where CFCs have not yet penetrated. From the TTDs, we calculate the ideal mean age, Γ, the TTD width, Δ, and the mass fraction of water with transit times less than a century, f_1. We also quantify the entropic uncertainties due to the nonuniqueness of the deconvolutions. In the Atlantic, the patterns of Γ and f_1 reflect the distribution of the major water masses. At the deepest locations in the North Atlantic $\Gamma \simeq 300^{+300}_{-100}$ a, while at the deepest locations in the South Atlantic $\Gamma \simeq 500^{+200}_{-100}$ a. The Pacific is nearly homogeneous below 2000 m with $\Gamma \simeq 1300^{+200}_{-50}$ a in the North Pacific and $\Gamma \simeq 900^{+200}_{-100}$ a in the deep South Pacific. The Southern Ocean locations have little vertical structure, with Γ ranging from 300 to 450 a with an uncertainty of about $^{+150}_{-40}$ a. The importance of diffusion compared to advection as quantified by Δ/Γ has most probable values ranging from 0.2 to 3 but with large entropic uncertainty bounds ranging from 0.2 to 9. For the majority of locations analyzed, the effect of ^{39}Ar is to reduce f_1 and to correspondingly increase Γ by about a century. The additional constraint provided by ^{39}Ar reduces the entropic uncertainties of f_1 by roughly 50% on average.

1.   Introduction

[2]   Transport from the mixed layer into the ocean interior is fundamentally quantified by the boundary propagator Green function, $\mathcal{G}$, an integral representation of the ocean's transport operator for transport from the surface. (We emphasize that the real ocean has a transport operator, not just ocean models.) Because the tracer concentrations at an interior point are convolutions in time and space of the mixed layer concentrations with the boundary propagator, tracer measurements in the ocean interior provide data constraints on $\mathcal{G}$, and hence on oceanic transport from the surface. Here we apply a maximum entropy (ME) method to hydrographic bottle data to deconvolve for $\mathcal{G}$. Physically, every fluid element in the bottle carries the tracer concentration of the mixed layer from the time and place when the fluid element was last in contact with the

surface. The concentration measured for the bottle represents an admixture of these fluid elements, each of which has taken a different advective-diffusive path, with a different transit time, from the surface to the bottle. When integrated globally or regionally over source locations, the boundary propagator reduces to the transit time distribution (TTD), which is the distribution of the transit times from the surface represented by the collection of fluid elements in the bottle.

[3]   Deconvolution of tracer data for the boundary propagator at a given point in the ocean interior is highly underdetermined: For a given interior bottle location $\mathcal{G}$ must be determined for each time and location of possible last surface contact using only a few tracers, typically sampled sparsely in time and space. In particular, only a few tracers constrain the transit time dependence of $\mathcal{G}$. For global coverage the chlorofluorocarbons (CFCs) and radiocarbon are the only readily available candidates, although the CFC's have not penetrated into the deep ocean everywhere. The CFC's and radiocarbon encode timescales that are separated by 2 orders of magnitude, with CFCs only going back some 70 years with an effective half-life of approximately 30 years and radio carbon with a half-life of 5730 years. The cosmogenically produced radio isotope ^{39}Ar with a half-life of 269 years, roughly placed near the geometric mean of the CFC and radiocarbon timescales, is therefore an attractive tracer to bridge the gap in CFC and

[1]Department of Applied Mathematics, School of Mathematics and Statistics, University of New South Wales, Sydney, New South Wales, Australia.
[2]Also at Department of Applied Physics and Applied Mathematics, Columbia University, New York, New York, USA.
[3]Department of Earth System Science, University of California, Irvine, California, USA.

radiocarbon timescales. Because of its low abundance, traditional methods of determining the ^{39}Ar concentration require large water volumes, and available data are therefore sparse. Nevertheless, new analytic techniques [e.g., *Gaelens et al.*, 2005; *Welte et al.*, 2010] may make ^{39}Ar concentrations more widely available and it is worth quantifying how estimates of $\mathcal{G}$ are improved when ^{39}Ar is available. In this paper we ask the following key questions: (1) What do the deconvolutions of oceanic tracers, including ^{39}Ar, reveal about ocean transport in terms of basic diagnostics such as ideal mean age, and the mass fraction of water in certain transit time classes? (2) How does the inclusion of ^{39}Ar change the results of maximum entropy deconvolutions of TTDs and what are the systematics of these changes? (3) To what degree does the additional information carried by ^{39}Ar reduce the uncertainty associated with the underdetermined nature of the deconvolution problem?

[4] To this end we apply ME deconvolutions to the ^{39}Ar data obtained by *Loosli* [1989] as tabulated in the thesis of *Rodriguez* [1993], in conjunction with CFCs and natural ("prebomb") radiocarbon from the GLODAP data set [*Key et al.*, 2004; *Sabine et al.*, 2005], and potential temperature, θ, salinity, S, and the quasi-conserved tracer PO$_4$* $\equiv$ PO$_4$ + O$_2$/175 [*Broecker et al.*, 1998] as computed from the World Ocean Atlas 2005 (WOA05) [*Locarnini et al.*, 2006; *Antonov et al.*, 2006; *Garcia et al.*, 2006a, 2006b].

[5] The value of ^{39}Ar as a transport tracer has been recognized in previous studies. *Maier-Reimer* [1993] used a simple argument based on one-dimensional advection-diffusion to interpret the ^{39}Ar–^{14}C scatter diagram as carrying distinct signatures for advective and diffusive transport. [*Broecker and Peng*, 2000] contrast ^{39}Ar and ^{14}C ages in the deep ocean assuming two end members whose proportions were inferred from the distribution of PO$_4$* and attribute the difference between these tracer ages to diffusive mixing. Our approach emphasizes the estimation of tracer-independent transport diagnostics intrinsic to the flow by deconvolving tracer concentrations for the ocean's boundary propagator.

2. Deconvolution Method

[6] The ME method as applied to deconvolving tracer data to determine the boundary propagator was described in detail in the work of *Holzer et al.* [2010], which we now summarize: The concentration $C_j^I(\mathbf{r}, t)$ of passive tracer species j at $(\mathbf{r}, t)$ is the admixture of surface concentrations from surface points $\mathbf{r}_s$ at earlier times t' given by the convolution

$$C_j^I(\mathbf{r}, t) = \int d^2 r_s \int_{-\infty}^{t} dt' \mathcal{G}(\mathbf{r}, t | \mathbf{r}_s, t') C_j^S(\mathbf{r}_s, t') e^{-\gamma_j(t-t')}, \quad (1)$$

where the boundary propagator Green function $\mathcal{G}$ is an integral representation of the transport from the surface [e.g., *Holzer and Hall*, 2000], and γ_j is the decay constant for radioactive species ($\gamma_j = 0$ for nonradioactive species). The superscripts I and S emphasize interior and surface tracer concentrations, respectively. Assuming the ocean to be cyclostationary and discretizing time into 12 month per year, the discretized version of $\mathcal{G}d^2 r_s dt'$ is the

probability $\mathcal{P}(s, n, m | \mathbf{r}, m_0)$. In terms of $\mathcal{P}$ the convolution (1) becomes

$$C_j^I(\mathbf{r}, t) = \sum_{s} \sum_{n=0}^{\infty} \sum_{m=1}^{M(n)} \mathcal{P}(s, m, n | \mathbf{r}, m_0) C_j^S(s, t - \tau_{n,m}) e^{-\gamma_j \tau_{n,m}}$$
$$\equiv \hat{C}_j^I[\mathcal{P}], \quad (2)$$

where $\tau_{n,m} = [n + (m_0 - m)/12]\tau_a$ with $\tau_a = 1$a and $M(0) = m_0$ and $M(n) = 12$ for $n > 0$. Equation (2) also defines the notation $\hat{C}_j^I[\mathcal{P}]$ for the value of the interior tracer concentration obtained by propagating the boundary conditions C_j^S with a given $\mathcal{P}$. Physically, $\mathcal{P}(s, n, m | \mathbf{r}, m_0)$ is the mass fraction of water at $\mathbf{r}$ during month m_0 that had last contact with the sth surface patch n years previously during month m, and thus had a transit time $\tau_{n,m}$ from the surface to the point of observation. Equivalently, $\mathcal{P}(s, n, m | \mathbf{r}, m_0)$ is the probability that a fluid element at $\mathbf{r}$ had a transit time $\tau_{m,n}$ since last surface contact with patch s, conditional on the fluid element currently being at $\mathbf{r}$ during month-of-year m_0. To account for all the water at $(\mathbf{r}, m_0)$, $\mathcal{P}$ has the normalization $\sum_{s,n,m} \mathcal{P}(s, m, n | \mathbf{r}, m_0) = 1$. For less cumbersome notation below, we will also use the abbreviated notation $\mathcal{P}(s, \tau | \mathbf{r}) \equiv \mathcal{P}(s, n, m | \mathbf{r}, m_0)$.

2.1. Information Entropy, $\mathcal{S}$

[7] Following *Jaynes* [1957], we now assert that the best choice for $\mathcal{P}$ is that which is maximally noncommittal with regard to missing information by maximizing the information entropy $\mathcal{S}$ [*Shannon*, 1951] subject to any data constraints. Enforcing the data constraints with Lagrange multipliers λ_j, the information entropy of $\mathcal{P}$ takes the form

$$\mathcal{S} = -\sum_{s,n,m} \mathcal{P} \log \frac{\mathcal{P}}{\mu} + \sum_{j=1}^{J} \lambda_j \left(C_j^I - \hat{C}_j^I[\mathcal{P}] \right). \quad (3)$$

In (3) the measure, or "prior", μ provides a prior guess at $\mathcal{P}$ in the sense that the maximum of $\mathcal{S}$ in the absence of data constraints is $\mathcal{P} = \mu$. By setting the functional derivative of $\mathcal{S}$ with respect to $\mathcal{P}$ to zero it follows that $\mathcal{S}$ is maximized by

$$\mathcal{P} = \frac{\mu}{Z} \exp\left(-\sum_{j} \lambda_j C_j^S(s, t - \tau_{n,m}) e^{-\gamma_j \tau_{n,m}} \right), \quad (4)$$

where Z normalizes $\mathcal{P}$. The J Lagrange multipliers are found by substituting (4) into the J constraints (2). This results in equations that are nonlinear in the λ_j, that are then solved numerically. (Note that while the normalization of $\mathcal{P}$ could formally be imposed with an additional Lagrange multiplier, normalizing the ME solution subject to only the data constraints is mathematically equivalent.)

[8] As in the work of *Holzer et al.* [2010], we consider both a uniform prior and a prior based on coarse resolution solutions of a steady advection-diffusion equation. We refer to the latter as the advective-diffusive (AD) prior. The uniform prior has the property that in the absence of any information all surface locations and all times since last contact, up to a maximum time $\tau_{\max} = 20000$a, are equally

likely. The details of how the priors were constructed can be found by *Holzer et al.* [2010]. Additional details on how transit time was discretized is provided in Appendix A.

2.2. Entropic Distribution

[9] To quantify the uncertainty associated with the underdetermined nature of finding $\mathcal{P}$, one must be able to assign a probability to functions $\mathcal{P}$ that do not maximize the constrained entropy, but that still satisfy the data constraints. We assume here that the uncertainty associated with the underdetermined nature of the inversion is the dominant uncertainty and ignore instrumental error and uncertainty due to temporal variability in the data. Support for this assumption has been provided by Monte Carlo simulations of ME inversions of WOCE line A20 data [*Holzer et al.*, 2010]. In the case of negligible data uncertainty the probability distribution of $\mathcal{P}$ can be argued [e.g., *Skilling and Gull*, 1991; *Press et al.*, 2007] to take the form

$$p(\mathcal{P}) \propto \exp\left(-\frac{N}{2}\frac{\mathcal{S}[\mathcal{P}]}{\mathcal{S}_{\max}}\right), \qquad (5)$$

where $\mathcal{S}_{\max}$ is the maximum of the data-constrained entropy, and N is the number of effective constraints on $\mathcal{P}$ provided by the data. Equating N with the number of constraints [e.g., *Gull and Daniell*, 1978] is the choice of the so-called "classic" maximum entropy method [e.g., *Skilling and Gull*, 1991]. Here we take $N = J$, the number of tracer constraints used. Thus, when all the tracers considered (T, S, PO_4^*, CFC-11, CFC-12, ^{14}C, and ^{39}Ar) are available for a given location, $N = 7$.

[10] Typically we wish to determine the probability density function (pdf) of a diagnostic $\hat{D}[\mathcal{P}]$ that can be obtained as a moment of $\mathcal{P}$, that is, $\hat{D}[\mathcal{P}] = \sum_{s,m,n} \mathcal{P}(s, n, m|\mathbf{r}, m_0)F(s, n, m)$, for a suitable function $F(s, n, m)$. An example is $\hat{D} = \Gamma$, the ideal mean age for which $F = \tau_{n,m}$. The pdf of $\hat{D}$ taking a particular value in the interval $(D, D + dD)$ is given by equation (5), where the entropy $\mathcal{S}[\mathcal{P}]$ is computed for a propagator $\mathcal{P}$ that is forced to satisfy the additional constraint that $D = \hat{D}[\mathcal{P}]$, which we add to the constraints of equation (3) with the additional Lagrange multiplier term $\lambda_D(D - \hat{D})$. (The maximum data-constrained entropy, $\mathcal{S}_{\max}$ corresponds to the value of D for $\lambda_D = 0$.)

[11] Finding $p(D)$ requires solving $J + 1$ nonlinear equations for the Lagrange multipliers for each value of D. To reduce the computational burden, we proceed as in the work of *Holzer et al.* [2010] and compute the entropy $\mathcal{S}(D)$ only at two values of D on each side of the ME value of D^* and use these points to fit $\mathcal{S}$ to a power law $\mathcal{S} = b|D - D^*|^a$ separately on each side of the maximum. We summarize the width of $p(D)$ in terms of half-width and probability-based error bars. The half-width error bar stretches from the left to the right half-peak value of $p(D)$. The probability-based error bar stretches from D_L to D_R, where $\int_{-\infty}^{D_L} p(D)dD = 0.5 \int_{-\infty}^{D^*} p(D)dD$, and $\int_{D_R}^{\infty} p(D)dD = 0.5 \int_{D^*}^{\infty} p(D)dD$. In other words the probability error bars stretch from half the cumulative probability to the left of the ME value D^* to half the cumulative probability to the right of D^*. For a symmetric distribution D_L and D_R locate the left and right

quartiles of the distribution. In all cases, the probability of D lying in the range of the probability error bar is 0.5, that is, $\int_{D_L}^{D_R} p(D)dD = 0.5$. For convenience, we refer to the probability-based error bars as quartile error bars, even in the case of asymmetric distributions.

3. Data

[12] The ^{39}Ar data used in this study was taken from the doctoral thesis of *Rodriguez* [1993], which tabulates 125 ^{39}Ar measurements taken by Hugo Loosli and collaborators during the 1980s and early 1990s. The data is sparse because the low abundance of ^{39}Ar required thousand liter samples for the counting of electrons produced by the radioactive decay at a rate of only a few per hour for surface water samples. The analytical techniques are discussed by *Loosli* [1983], and the data are discussed by *Schlitzer et al.* [1985] and *Rodriguez* [1993]. The data are in the form of the ratio of ^{39}Ar to total Ar in the water sample relative to the $^{39}Ar/Ar$ ratio in the atmosphere, that is, $\chi_{Ar} \equiv (^{39}Ar/Ar)_{sample}/(^{39}Ar/Ar)_{atmos.}$, and carries a typical uncertainty of about 5%. Because of the rapid air-sea exchange of argon, solubility plays no role and the surface can be considered to be saturated [e.g., *Maier-Reimer*, 1993]. We therefore treat χ_{Ar} as a passive tracer with a surface boundary condition of $\chi_{Ar} = 1$, independent of surface location. Because the focus of this study is on the constraints provided by ^{39}Ar, we perform the ME inversions at the locations where the water samples analyzed for ^{39}Ar data were obtained.

[13] The other time-dependent tracers employed are CFC-11, CFC-12, and natural ("prebomb") ^{14}C, whose annual mean interior and surface concentrations are taken from the GLODAP data set [*Key et al.*, 2004; *Sabine et al.*, 2005]. For the surface boundary conditions, the smaller GLODAP domain was extended to that of the WOA05 domain, as described by *Holzer et al.* [2010]. Where gridded CFC concentrations fell below the detection limit, the CFC data was not used. The time-evolving CFC boundary conditions were constructed as in the study of *Holzer et al.* [2010] by scaling the nominal 1994 GLODAP surface values to the other years using the time series of atmospheric CFC concentrations [*Walker et al.*, 2000]. Temperature, salinity, phosphate, and oxygen data were taken from the WOA05 [*Locarnini et al.*, 2006; *Antonov et al.*, 2006; *Garcia et al.*, 2006a, 2006b], with annual means for the interior concentrations, and monthly means for the surface boundary conditions.

[14] Argon data whose location fell outside the GLODAP domain were not considered. We also did not consider data in the upper 250 m of the ocean because our neglect of seasonal and interannual variability in the CFC and ^{14}C boundary conditions is particularly troublesome in the upper ocean. This leaves 70 ^{39}Ar measurements for which the other tracers are also available. The geographical locations of the tracer data sets used in this study are plotted in Figure 1. Of these we could not find a numerically exact maximum entropy inversion for 9 data points because of either data inconsistencies (no linear combination of the boundary values can result in the interior values) or numerical difficulties. We thus present results for 61 sets
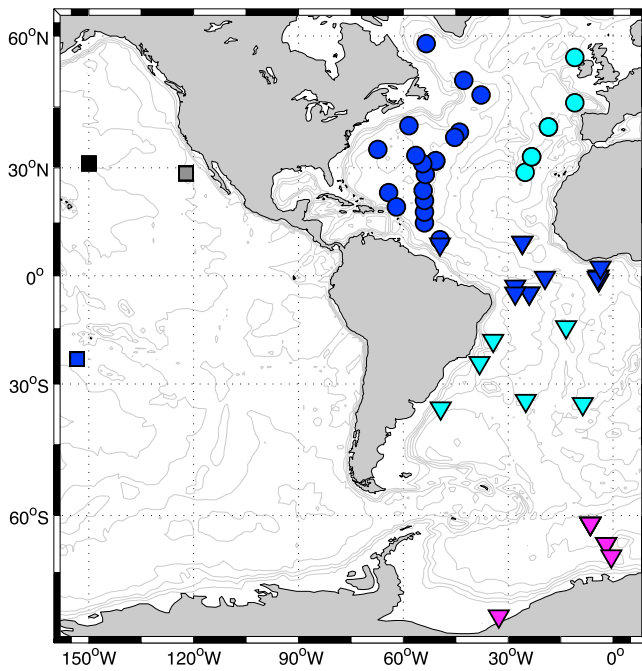
Figure 1. The locations of the ^{39}Ar measurements used in this study. Symbol shapes and colors are introduced to label different regions. Bathymetry is indicated in 1000 m intervals.

of tracer data, comparable to the number of ^{39}Ar data that were analyzed by *Broecker and Peng* [2000].

4. One-Dimensional Idealized Model

[15] Before analyzing the oceanographic data it is useful to consider a simple one-dimensional (1d) model to illustrate the role of ^{39}Ar in constraining TTDs and to provide a sense of the nature of the solutions and the entropic uncertainty.

[16] The boundary conditions at the sea surface for the four time-dependent tracers CFC-11, CFC-12, ^{14}C, and ^{39}Ar are specified as follows: For the CFCs we use the globally averaged atmospheric concentrations taken from the work of *Walker et al.* [2000], scaled to some suitable mixed layer concentration, which is arbitrary here. For ^{14}C, and ^{39}Ar we have $C_j^S(\tau) = \exp(-\gamma_j \tau)$, where the decay rate constant $\gamma_j = \ln(2)/t_j^*$, with half lives $t_{Ar}^* = 269$a and $t_C^* = 5730$a. These idealized boundary conditions are shown in Figure 2. Note that the surface concentration of the CFCs is identically zero for $\tau > 70$a, which has consequences for the inversions as discussed below.

[17] Synthetic interior tracer concentrations were generated by convolving these boundary conditions with a model boundary propagator that is independent of surface location, that is, with a model TTD. The natural choice is an inverse Gaussian (IG), $\mathcal{G}_{IG}$, which is also a solution to the 1d advection diffusion equation [e.g., *Hall and Plumb*, 1994]. The IG is a function of two parameters, its mean age Γ and its width Δ. The mean age parameter can be thought of as being proportional to depth, z: For constant coefficient advection-diffusion with advection speed v one has $z = v\Gamma$. The mode of $\mathcal{G}_{IG}$, that is, the time τ_m for which $\mathcal{G}_{IG}$ is

peaked is given by $\tau_m = \left(\sqrt{1 + (3/Pe^2)^2} - 3/Pe^2 \right) \Gamma$, where $Pe \equiv \Gamma/\Delta$ is the Péclet number of the 1d flow.

[18] Given the boundary conditions and the synthetic data for a given Γ and Pe, we can then imagine that the boundary propagator is unknown and use the ME deconvolution to provide an estimate for $\mathcal{G}$, which can then be compared against the true answer, our assumed IG. The ME deconvolutions for this 1d model were performed using a uniform prior out to $\tau = 20000$a.

[19] Figure 3 shows the deconvolved TTDs with and without ^{39}Ar compared to the true model $\mathcal{G}_{IG}$ for Pe = 1.5 and Pe = 10. A value of Pe = 1.5 is thought to be typical of the real ocean ([e.g., *Waugh et al.*, 2004] and see below), while Pe = 10 represents more advectively dominated flow. The main message of Figure 3 is that without ^{39}Ar, the ME solution for the TTD cannot form a mode beyond the CFC period of ~70a: Without ^{39}Ar the tail of the ME solution for $\tau > 70$a is determined only by ^{14}C, and because the TTD must approach zero for large τ the Lagrange multiplier of ^{14}C must be positive, which implies that the TTD decreases monotonically for $\tau > 70$ a. On the other hand if both ^{39}Ar and ^{14}C are available, the Lagrange multipliers of the two tracers can be of opposite sign, allowing the solution to have both growth and ultimate long-τ decay beyond the CFC period so that a mode at long τ is possible. This is particularly evident for Pe = 10, but also visible at large mean ages for Pe = 1.5.

[20] Figure 3 allows us to emphasize another important point: Even with error-free tracer data, such as used in this example, one cannot expect the ME deconvolutions to recover the true underlying TTD with only a handful of tracer constraints. The ME solution is the exponentiated linear combination of the surface values of the few available tracers as expressed by equation (4). While this solution guarantees to satisfy the available tracer constraints (2), constraining the functional shape of the TTD amounts to constraining the TTD for an infinite number of transit times. (Alternatively, constraining the detailed functional form of the TTD is equivalent to constraining an infinite number of its moments.) Thus, the ME deconvolution can only recover the underlying TTD exactly for an infinite number of (independent) tracer constraints. The fact that the ME deconvolution is able to provide an estimate of the functional form of the TTD with only a few tracer constraints is due to the smoothing property of the entropy functional [e.g., *Press et al.*, 2007], which spreads out the probabilities $\mathcal{P}$ as much as possible relative to the prior μ. The functional form of the ME deconvolutions (4) is not constrained to be unimodal and is therefore in principle able to capture multimodal TTDs arising from multiple advective-diffusive pathways. However, it must be kept firmly in mind that the functional shape constrained by only a few tracer observations has significant uncertainty and the detailed structure of the deconvolved TTD should not be overinterpreted as underscored by the spurious bimodality of the inversion for Pe = 1.5 and $\tau_m = 25$ a ($\Gamma = 75$a) in Figure 3. A key strength of the ME method is that we can quantitatively assess the uncertainty associated with the paucity of constraints.

[21] To illustrate the nature of the entropic uncertainty due to the underdetermined nature of the deconvolutions, we
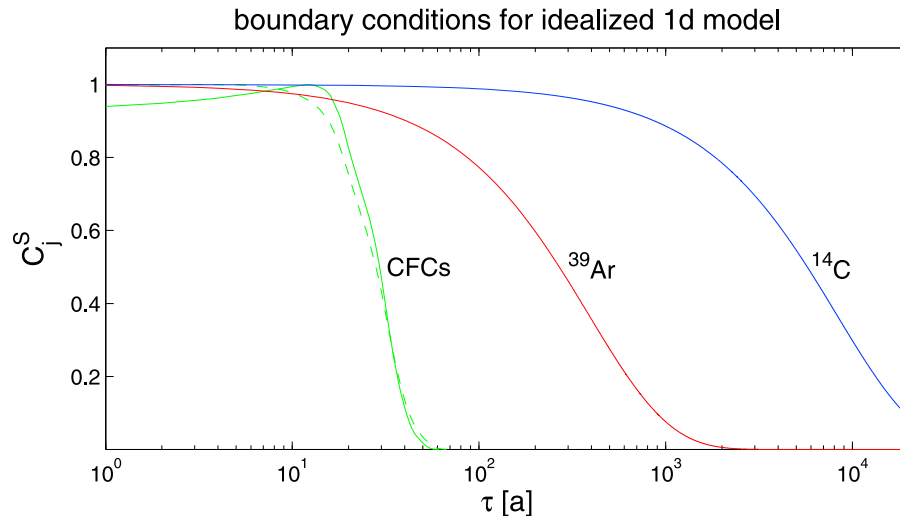
Figure 2. The effective surface boundary conditions for the idealized 1d model as a function of time since last surface contact, τ, for the four transient tracers considered: CFC-11 (green, solid), CFC-12 (green, dashed), ^{39}Ar (red), and ^{14}C (blue). The logarithmic time axis emphasizes that the ^{39}Ar timescale is roughly the geometric mean of the CFC and ^{14}C timescales.

focus on the mass fractions of water in the three transit time bands $[t_{min}, t_{max}) = [0, 100)$, $[100, 500)$, and $[500, 20000)$a, where the mass fraction is simply $f = \int_{t_{min}}^{t_{max}} d\tau \, \mathcal{G}(\tau)$. We denote the mass fractions in the three bands f_1, f_2, and f_3, with f_1 containing the youngest water, and f_3, the oldest. Note that $f_1 + f_2 + f_3 = 1$. Figure 4 shows the probability distributions for these fractions for Pe = 1.5, as obtained with and without ^{39}Ar for five different modal times τ_m (and hence five different ideal mean ages) of the underlying assumed IG TTD. The pdfs of the water mass fractions are generally quite broad, except where the ME values of f lie near the extremes of $f = 0$ or 1 (none or all the water in the band). This broadness reflects the fact that we are using only three or four data constraints to estimate a TTD of arbitrary functional form (as opposed to fixing the functional form from the outset and estimating only a few parameters). Including ^{39}Ar narrows the pdfs reflecting the additional constraint and the reduced entropic uncertainties in the maximum entropy values. Including ^{39}Ar generally also changes the maximum entropy value, but these changes are small compared to the width of the pdfs.

[22] To quantify the changes δf in the inferred water mass fractions in each transit time band due to the inclusion of ^{39}Ar, Figure 5 shows these changes as a function of the true ideal mean age, Γ, that is, the mean age of the assumed $\mathcal{G}$. Note that conservation of mass demands $\delta f_1 + \delta f_2 + \delta f_3 = 0$. For waters with $\Gamma \lesssim 750$a, inclusion of ^{39}Ar gives estimates with less water in the mid-τ band, and correspondingly more water in the short-τ and long-τ bands. For older ideal mean ages, inclusion of ^{39}Ar increases the long-τ content of the water at the expense of the mass fraction in the short-τ and mid-τ bands.

[23] The ideal mean age of the deconvolved TTD is surprisingly close to the true mean age of the assumed model transport. The discrepancy between inferred and true mean age for Pe = 1.5 is only about 2% when ^{39}Ar is not used, and less than 1% when ^{39}Ar is used. Though less relevant

for the real ocean, at Pe = 10 the discrepancy without ^{39}Ar can be several percent for waters with young ideal mean ages, but with ^{39}Ar becomes negligible for $\Gamma \gtrsim 150$a.

5.   Deconvolutions of Hydrographic Data

[24] Because our focus here is on the utility of ^{39}Ar for which the surface boundary conditions were approximated as perfectly uniform, we consider here only the temporal structure of the boundary propagator. In particular, we focus on the mass fraction f_1 of water younger than $\tau_1 \sim 105$a and on the mean and centered second moment of the distribution of transit times since last contact anywhere on the surface (TTD). (Note that the mass fraction older than τ_1 is simply $1 - f_1$.) We first present these diagnostics as computed using the AD prior and all available tracer constraints, including ^{39}Ar, that is, we first analyze our results obtained using the maximum available information. We then systematically investigate the effect of ^{39}Ar by comparing the diagnostics and their uncertainties computed with and without ^{39}Ar and with each prior.

5.1.   Oceanographic Significance of the Results With ^{39}Ar

[25] Figure 6 shows the inversion results for the mass fraction, f_1, of water with $\tau \in [0, 105)$ a for all the bottles below 250 m separately for the North Atlantic, South plus Equatorial Atlantic, Pacific and Southern Ocean basins. To a first approximation, we can consider the plots to represent vertical profiles for each basin, but we note that for each basin data from all latitudes and longitudes has been collapsed onto a single plot. (Only for the Pacific does the data actually consist of three vertical profiles at the locations shown in Figure 1.)

[26] The f_1 profiles reveal important differences in the water mass structure and ventilation pathways of the different basins. In the North Atlantic the vertical structure of
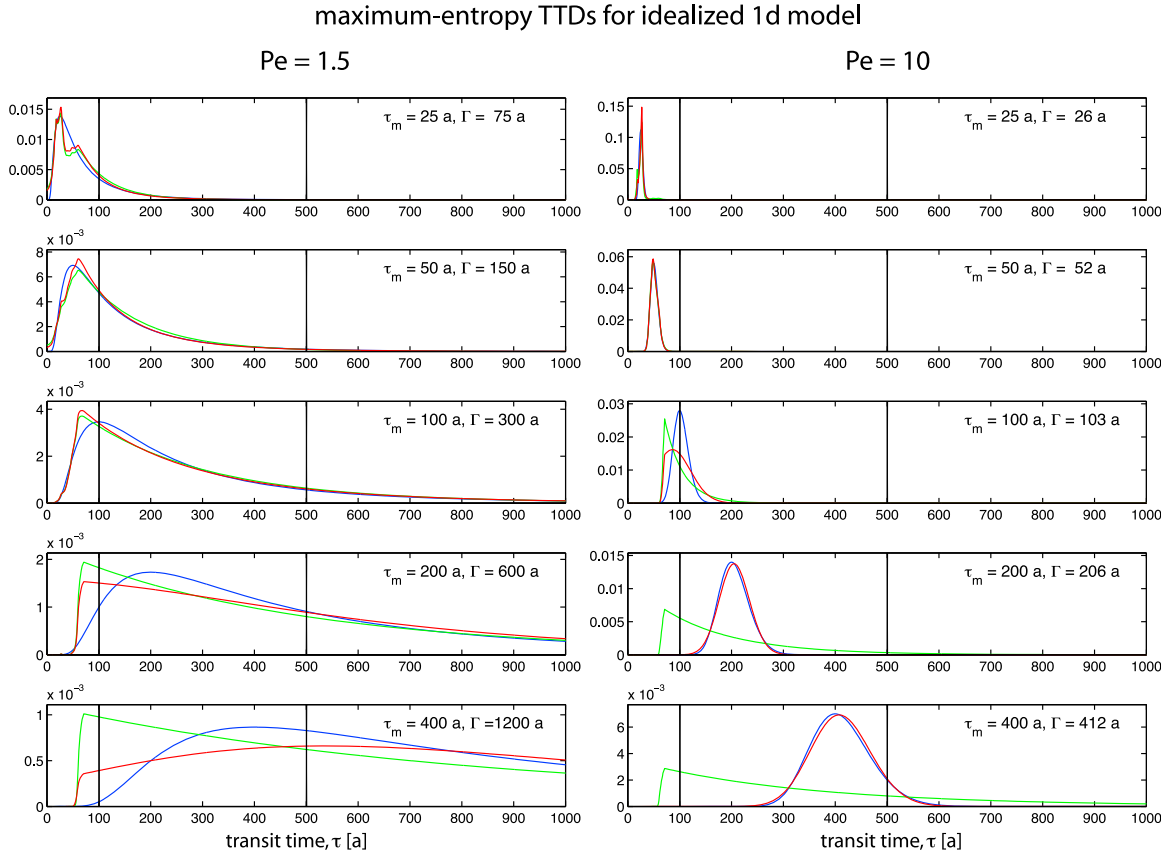
Figure 3. The ME TTD solutions for the idealized 1d model. The ME TTDs are plotted in green (no ^{39}Ar) and red (with ^{39}Ar), while the underlying exact TTDs are plotted in blue. The exact TTDs were convolved with the idealized boundary conditions of Figure 2 to generate the synthetic tracer data used by the ME inversions. The exact TTDs are characterized by (left) Pe = 1.5, and (right) Pe = 10. For each Pe, five exact TTDs with different mean ages Γ (and hence different modes, τ_m) were used as indicated. The vertical black lines are the boundaries of the three transit time bands considered to define τ-integrated water mass fractions.

f_1 as revealed by our inversions is consistent with what one expects given the known distribution of the ocean's major water masses. Relatively large values of f_1 are found between ~2000 and ~4000 m depth, where North Atlantic Deep Water (NADW) separates Antarctic Intermediate water (AAIW) above from Antarctic Bottom Water (AABW) below. (These water mass identifications were checked to be consistent with density (not shown).) The longer transit time from the surface of the Southern Ocean to the North Atlantic for AAIW and AABW is reflected in the relatively smaller f_1 values for the deepest bottles (AABW) and for the two bottles at 850 m depth (AAIW). The data point with $f_1 \sim 0.9$ at 680 m depth comes from the center of the Labrador Sea, a well known deep water formation site where we expect to find recently ventilated water with f_1 near unity. Consistent with the longer

time needed for NADW to be transported into the South Atlantic, the values of f_1 for the South and Equatorial Atlantic in the depth range where one would expect to find NADW has generally decreased from the corresponding North Atlantic values. In contrast, f_1 values at ~900 m depth have increased, consistent with AAIW being closer to its source in the South and Equatorial Atlantic than in the North Atlantic. The Pacific profiles are consistent with the notion that the thermocline waters of the North Pacific are ventilated by subduction, downward Ekman pumping, and relatively shallow convection, whereas the deep Pacific waters are ventilated from remote deep water formation sites in the Southern Ocean and North Atlantic. The Pacific f_1 values are seen to decrease with depth down to about ~1000 m below which f_1 is near zero. For the profile near Baja California at

Figure 4. The entropic pdfs of the water mass fractions in the three transit time bands $\tau \in [0, 100)$a, $\tau \in [100, 500)$a, and $\tau \in [500, 20000]$a for the idealized 1d model with Pe = 1.5 (green for the case without ^{39}Ar, red for the case with ^{39}Ar). Each row of plots is for a different underlying assumed IG boundary propagator characterized by the modes τ_m indicated (for Pe = 1.5 one has $\Gamma = 3\tau_m$). The black dash-dotted vertical lines indicate the exact water mass fractions of the IG propagators, and the green and red vertical lines indicate the maximum entropy values at the maxima of the corresponding pdfs.
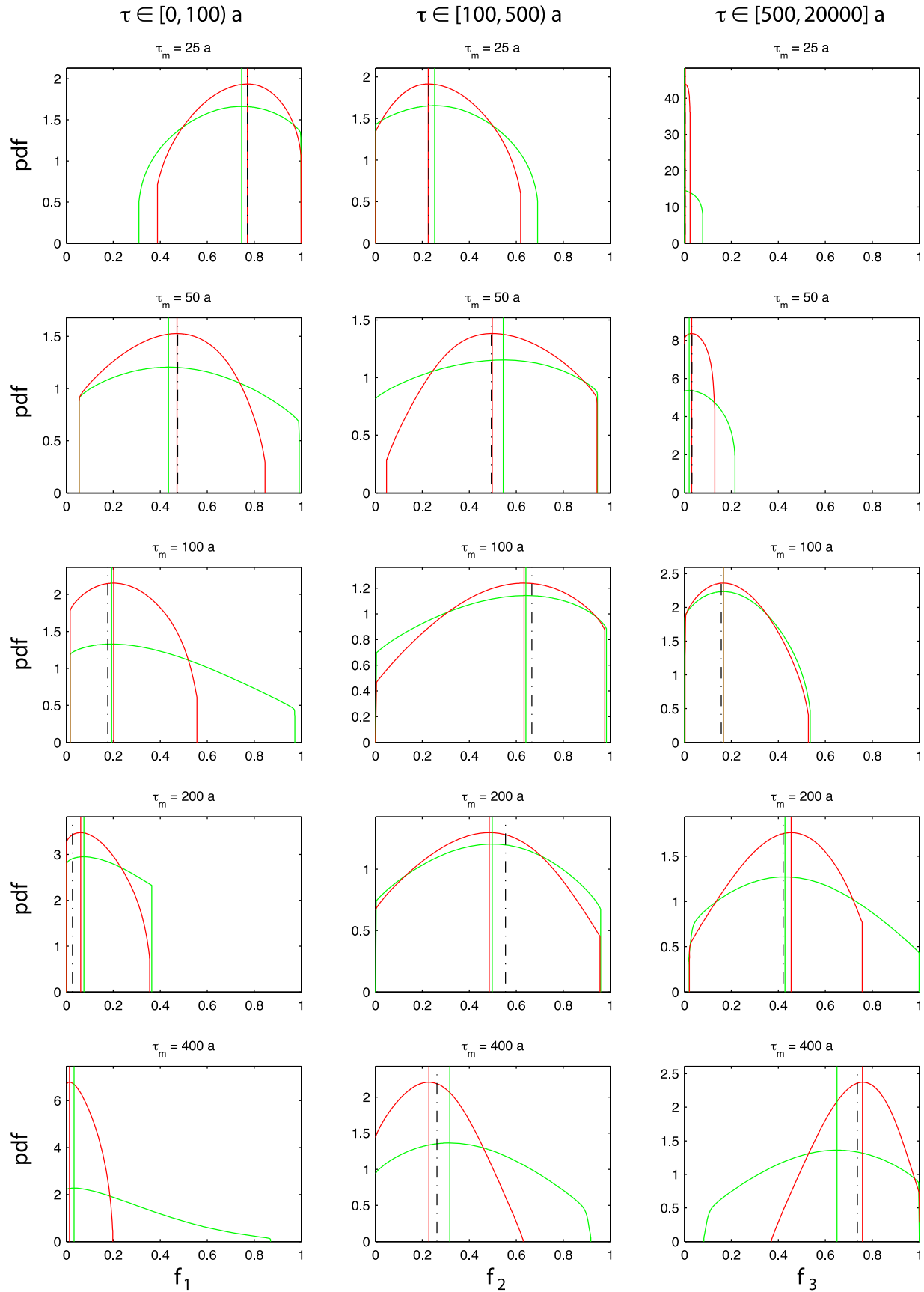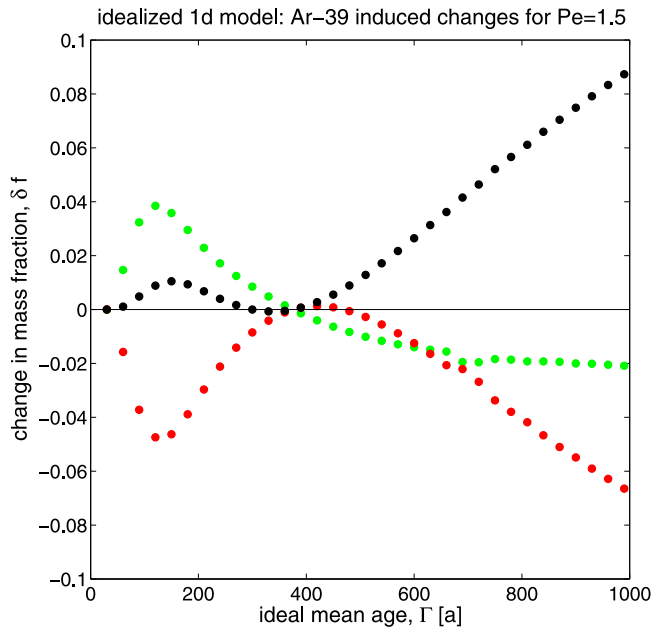
Figure 4

Figure 5. The change, δf, of the water mass fractions (with ^{39}Ar minus without ^{39}Ar) in each transit time band for the idealized 1d model with Pe = 1.5 as a function of the true mean age, Γ, of the underlying TTD. The change in the water mass fraction with $\tau \in [0, 100)$a is plotted in green, with $\tau \in [100, 500)$a in red, and with $\tau \in [500, 20000]$a in black.

(28.5°N, 122.2°W, grey squares), the values of f_1 in the thermocline are significantly smaller than for the other two Pacific locations. The thermocline at the Baja location is thus relatively poorly ventilated, consistent with its proximity to the North Pacific shadow zone [*Luyten et al.*, 1983; *Gehrie et al.*, 2006]. In the Southern Ocean, apart from a suggestion that f_1 increases slightly with depth, the vertical structure is much more uniform than elsewhere. This is consistent with the fact that in the Southern Ocean we have both formation of deep waters and reexposure of older waters to the atmosphere. The somewhat larger mass fraction in the youngest transit time band found for the deepest Southern Ocean bottles, if taken at face value, is consistent with the ventilation of the bottom waters by shelf slope convection along the Antarctic coast and subsequent upward mixing with older overlaying waters [e.g., *Foster and Carmack*, 1976; *Orsi et al.*, 1999].

[27] Figure 7 shows our ME estimates for the ideal mean age, Γ, as a function of depth, again plotted separately for four ocean basins as in Figure 6. Both the results with and without ^{39}Ar are shown so that the uncertainty reduction due to ^{39}Ar can be seen. The smaller error bars obtained when ^{39}Ar is included are particularly apparent in the Pacific and Southern Ocean. We note that while including ever more tracer constraints would ultimately lead to zero uncertainty, the approach to this limit with a nonuniform prior is not guaranteed to be monotonic and a few of the error bars actually increase when ^{39}Ar is included. We now focus on the depth dependence of ideal mean age itself and then return in detail to the effect of ^{39}Ar as an extra constraint in section 5.2.

[28] The vertical structure of Γ seen in Figure 7 is broadly consistent with the structure that we saw for f_1 in Figure 6. In the North Atlantic the youngest mean ages are found in the core of NADW between 2000 and 3000 m. Water above and below this depth tends to have older mean ages consistent with AAIW and AABW, which must travel farther to reach the North Atlantic. In the South and Equatorial Atlantic, the youngest mean ages (where we have ^{39}Ar data) are found above 1000 m where one would expect to find AAIW (see also *Holzer et al.* [2010]). Mean ages in the South and Equatorial Atlantic tend to increase gradually with depth except perhaps below 4000 m, where there is a sharp increase, but the large uncertainties preclude any firm conclusions. It is interesting to note that the deepest water masses tend to be older in the South Atlantic than in the North Atlantic suggesting that there is a gradual entrainment of NADW as AABW flows northward into the North Atlantic. In the Pacific we find mean ages that tend to increase from a minimum at the surface to a maximum at a depth of ~2000 m, below which mean age remains fairly constant throughout the homogeneous deep Pacific water mass. Consistent with the idea that the deep Pacific is ventilated from the south, the mean ages tend to be younger in the South Pacific (blue squares) than in the North Pacific (black and gray squares). Interestingly, the age profiles of the two North Pacific locations are very similar in spite of their different f_1 profiles. This is consistent with the fact that the TTDs at (31.1°N, 150°W) are significantly broader in the thermocline than those near Baja California (see Figure 8 discussed below). In contrast to the other basins, ideal mean ages in the Southern Ocean are more uniform with depth again suggesting that the Southern Ocean is an important location for the blending of different water masses, and where deep waters are not only newly formed but where old waters are also reexposed to the surface.

[29] Figure 8 shows the width, Δ, of the TTD defined by $2\Delta^2 = \int_0^\infty (\tau - \Gamma)^2 \, \mathcal{G}(\tau)d\tau$. The uncertainties of Δ were estimated from the entropic uncertainties of $m_2 \equiv \int_0^\infty \tau^2 \, \mathcal{G}(\tau) \, d\tau$ as described in section B1. Larger widths imply a greater multiplicity of transit times from the sea surface. This can be achieved by having a larger multiplicity of paths and transport timescales from a single water mass formation region or by mixing water from multiple source regions. As a general rule, one expects higher-order moments to be less well constrained than lower-order moments (Γ being the first-order moment, or mean, and $2\Delta^2$ being the second-order moment). Consistent with this expectation, Δ is seen to have much greater uncertainty than Γ. Despite the large uncertainties, our inversions suggest that the widths tend to increase with depth except perhaps for the Southern Ocean where Δ is nearly uniform with depth. As a general rule of thumb, one expects a large correlation between Γ and Δ because older water masses with large Γ have had more time to mix and thus to produce broader TTDs with larger values of Δ. This correlation is seen most places, with the old deep waters of the Pacific and Atlantic having large values of Δ, although the uncertainties for the Atlantic bottom waters are so large that their true width could be considerably smaller. An interesting exception to the rule is the thermocline waters of the North Pacific, where the values of Δ are roughly the same as those at depth even though thermocline waters have much smaller mean age than deep waters. There
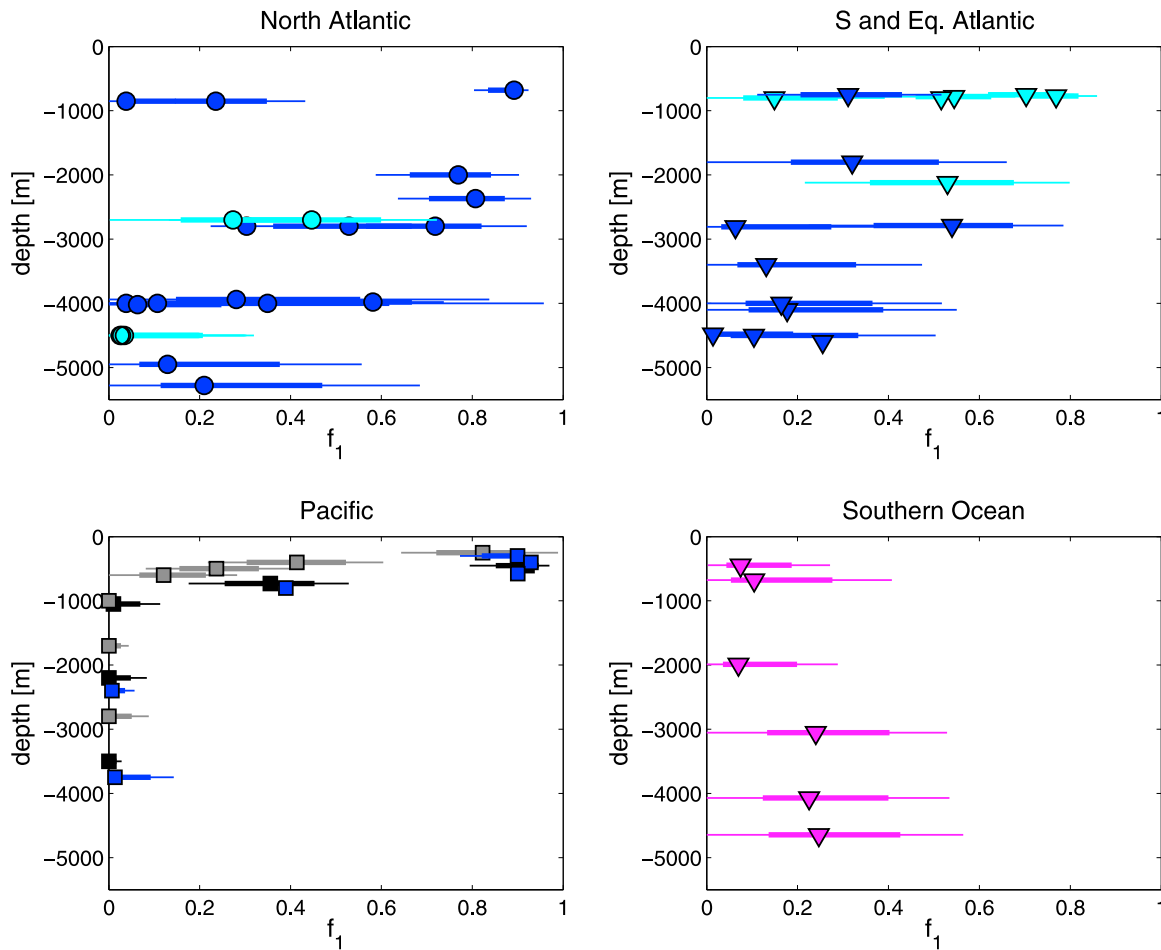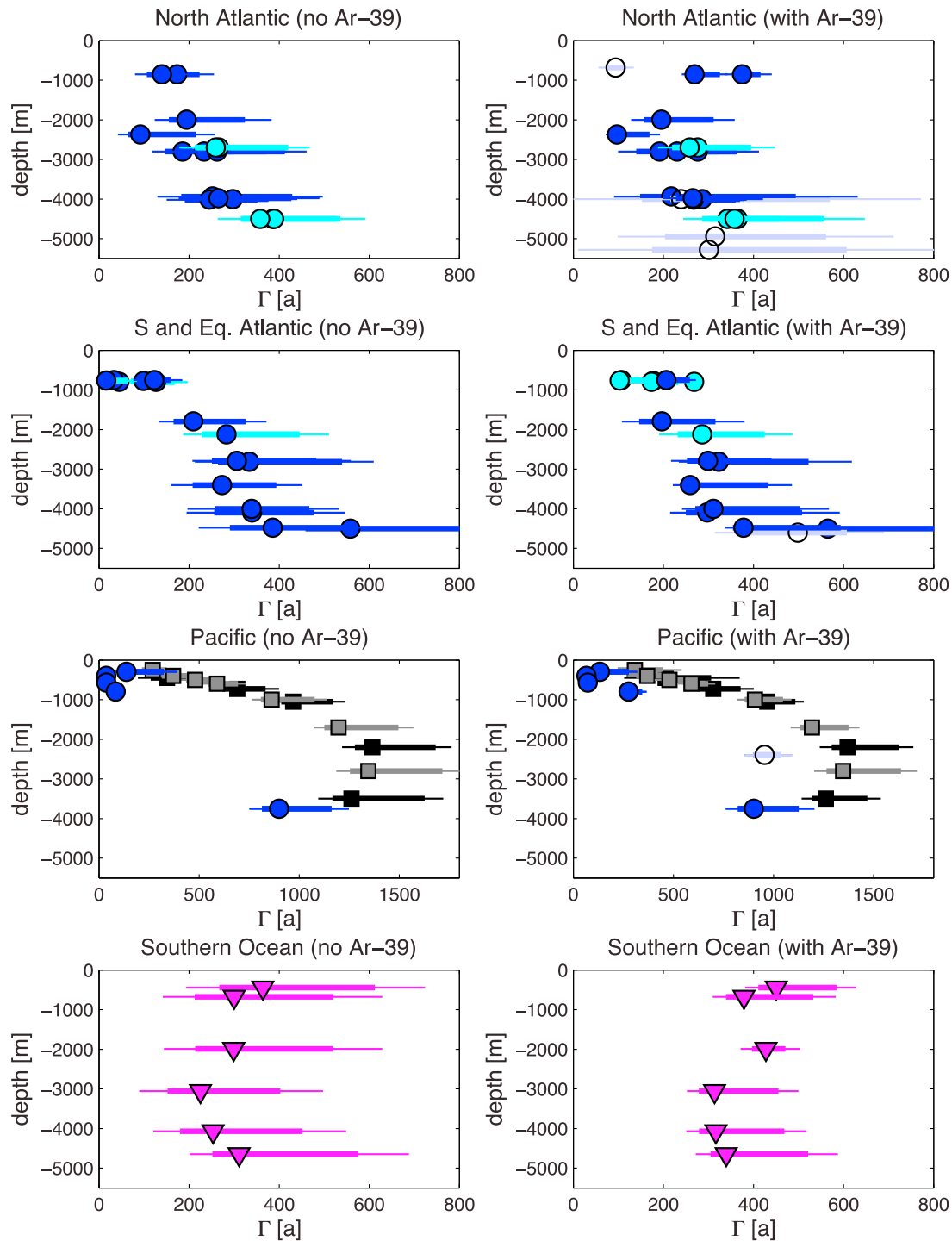
Figure 6. The mass fraction f_1 of water with transit time $\tau \in [0, 105)$a as determined using ^{39}Ar and the AD prior. Thick error bars cover half the probability of the associated entropic distribution, and thin error bars are associated with the width at half maximum of these distributions. Symbol shapes and colors identify the location of the ^{39}Ar measurements as in Figure 1.

is even a suggestion that the largest North Pacific values of Δ occur in the uppermost bottles analyzed, but the large uncertainties for these two bottles prevent definite conclusions. The weak dependence of Δ on depth in the North Pacific in spite of the strong vertical gradients of Γ above 2000 m suggests a subtle, complex structure of the TTDs in the North Pacific thermocline (see also Figure 10 below), perhaps resulting from upward diffusing older waters mixing with more recently ventilated water.

[30] The ratio of Δ/Γ is useful for characterizing the relative importance of diffusive and advective transport. If $\Delta/\Gamma \ll 1$, advection dominates over diffusion, while the converse is true if $\Delta/\Gamma \gg 1$. There have been few estimates of Δ/Γ from transient tracer data in the ocean. The only studies we are aware of are those of *Waugh et al.* [2003] and *Hall et al.* [2004], where measurements of CFC-11 and CFC-12 where used in conjunction to constrain both Γ and Δ. Because CFCs have relatively fast timescales, those studies could only estimate Δ and Γ for the relatively young water masses of the upper ocean where measurable CFC concentrations are present. Because we are using ^{39}Ar and ^{14}C tracer data in addition to the CFC data, we are able to

constrain Γ and Δ for deep waters as well. Furthermore, the previously estimated values of Δ/Γ were based on a parametric inversion approach in which the functional form of the TTD is assumed to be a two-parameter IG distribution that is completely specified given Γ and Δ. The IG approach turns an underdetermined problem into one that is exactly determined even with only two tracers whose timescales are similar. As such, the IG approach is poorly suited for quantifying what we call the entropic uncertainty, that is, the uncertainty in Δ/Γ associated with the fact that the functional form of the TTD is not known.

[31] In Figure 9 we plot estimates of Γ/Δ obtained from our ME inversions. (For convenience we plot Γ/Δ and its error bars rather than Δ/Γ so that a single scale suffices to show the error estimates in all basins.) While the corresponding ME estimates for Δ/Γ are generally greater than 0.2, the uncertainty is large and we cannot rule out a value of Δ/Γ as low as 0.1 in some locations. Nevertheless, it is generally true that eddy diffusive transport is significant everywhere and cannot be neglected. The so-called TTD method for estimating anthropogenic CO_2 in the ocean [e.g., *Waugh et al.*, 2006] generally assumes a value of Δ/Γ close

Figure 7. The ideal mean age, Γ, (left) without and (right) with ^{39}Ar and the AD prior. Thick error bars cover half the probability of the associated entropic distribution, and thin error bars are associated with the width at half maximum of these distributions. Symbol shapes and colors identify the location of the ^{39}Ar measurements as in Figure 1. Note that the Pacific has a different age scale. For Γ obtained with ^{39}Ar, open symbols with error bars in lighter color (four Atlantic and one Pacific location) indicate that the corresponding estimate without ^{39}Ar was not available because of numerical problems.

to unity. Within the framework of this TTD method, *Waugh et al.* [2006] report that anthropogenic CO_2 estimates are most sensitive to the assumed value of Δ/Γ when Δ/Γ is in the range between 0.2 and 0.8. For the upper ocean *Waugh*

et al. [2006] show that the CFC data is sufficient to exclude this range, but for deeper water our results suggest that values of Δ/Γ in the range between 0.2 and 0.8 cannot be ruled out.
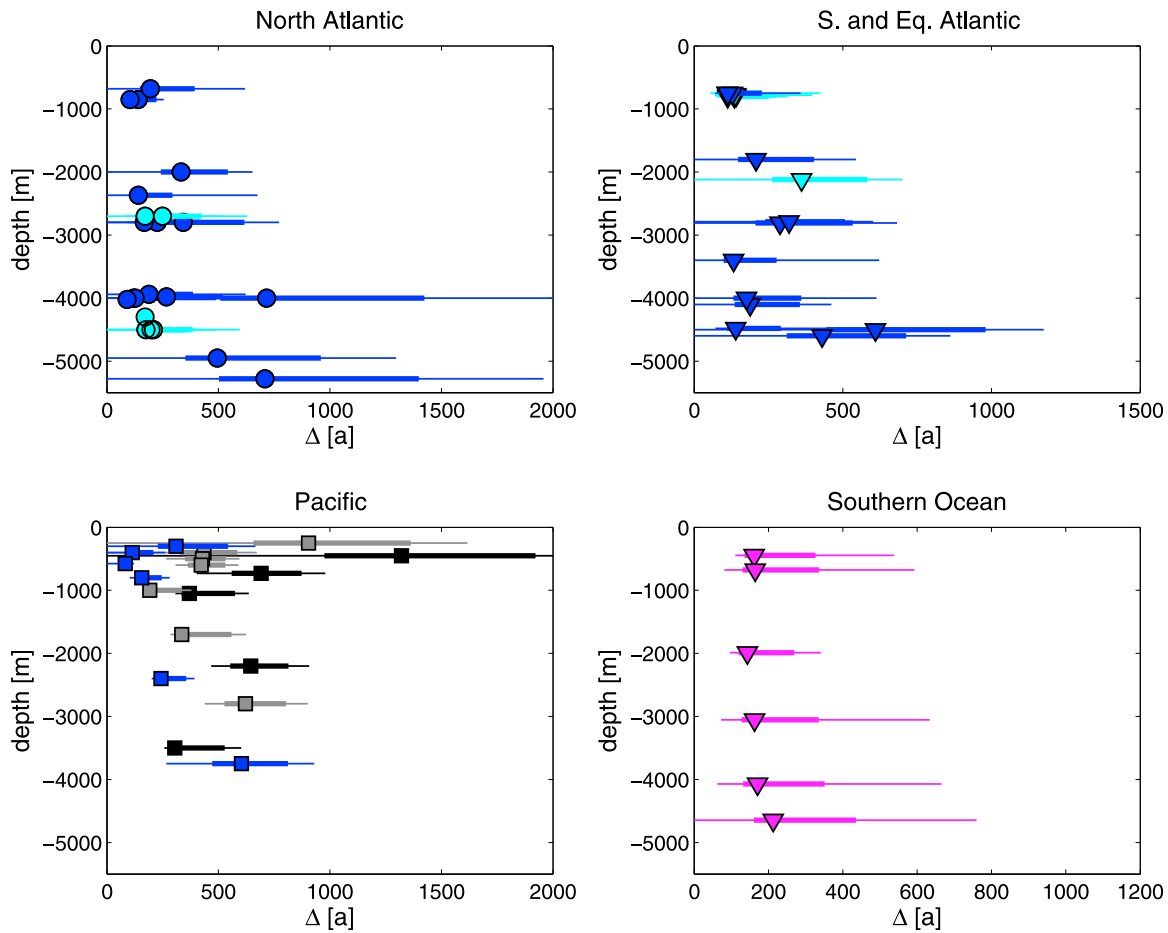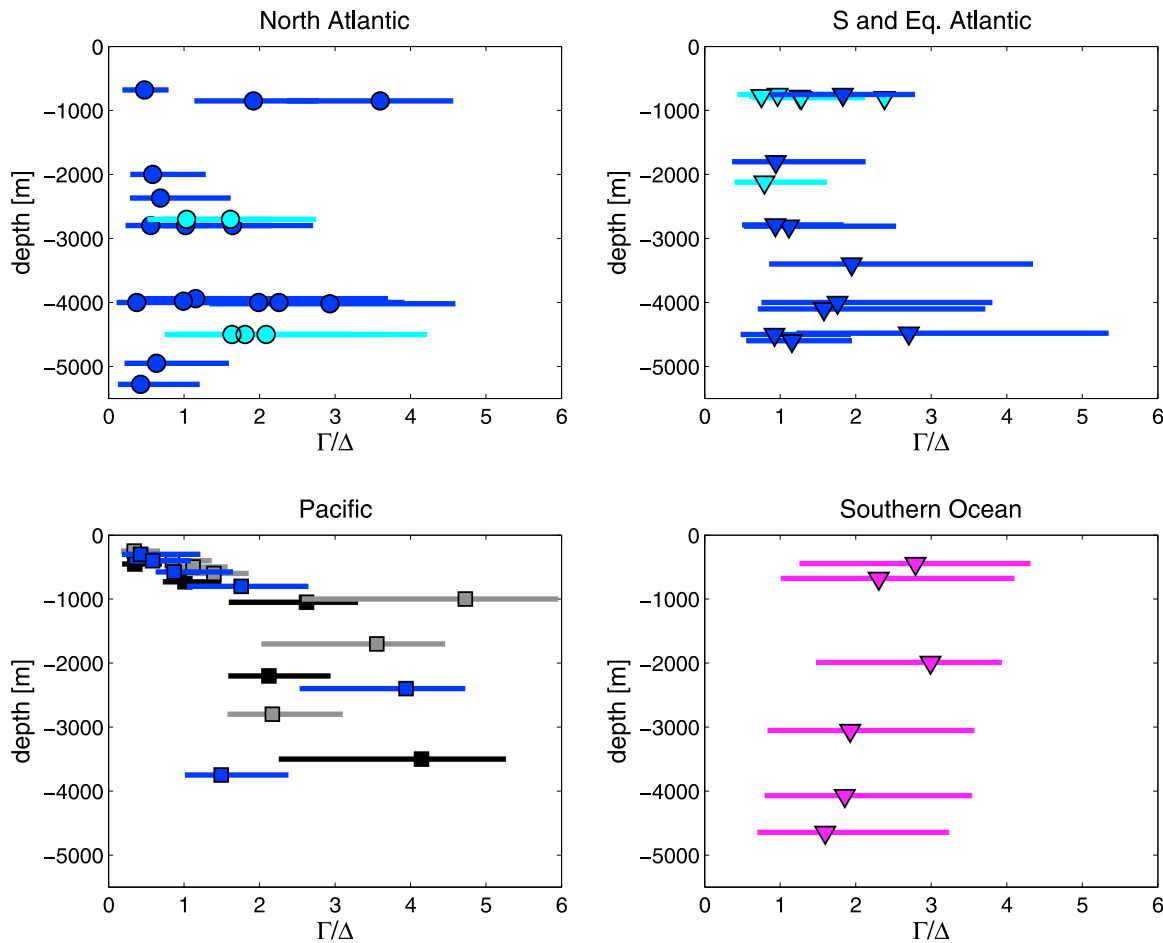
Figure 8. The TTD width, Δ, using [39]Ar and the model prior. Error bars were estimated as discussed in Appendix B. Symbol shapes and colors identify the location of the [39]Ar measurements as in Figure 1. Note that different basins have different scales for Δ.

[32] In Figure 10 we plot the ME TTDs (black curves) for the North Pacific station at 28.5°N, 122.2°W (Figure 10, top) and for the stations in the Southern Ocean (Figure 10, bottom). Superposed on each ME TTD is an IG distribution (red curves) with the same Γ and Δ as the ME TTD. Only for the North Pacific profile below the thermocline is there relatively good agreement between the IG distribution and the ME TTD. In the North Pacific thermocline above 600 m and for all depths in the Southern Ocean, the ME TTDs have an additional mode for $\tau \lesssim 50a$, which is absent in the less flexible IG distribution. It is difficult to know for certain if these short-τ modes are real or artifacts of the under-determined nature of the inversion. However, their existence does not contradict what is known about the ventilation of the ocean: In the North Pacific subduction of newly venti-lated water masses could easily explain the short-τ mode and in the Southern Ocean one expects to find recently ventilated water masses close to the deep water formation sites. It may be worth remarking that for most locations the TTDs of the corresponding AD prior (not shown) bear little resemblance to the ME TTDs. Details on the character of the AD prior TTDs may be found in the paper by *Holzer et al.* [2010].

5.2. Effect of [39]Ar as an Extra Constraint

[33] We now turn our attention to comparing ME inver-sions with and without [39]Ar to quantify the effect of includ-ing [39]Ar as an additional constraint. To this end, we focus on four key quantities: The mass fraction of water in each of the three transit time bands 0–105, 105–550, 550–20000a (band 1, 2, and 3), and the ideal mean age Γ. We refer to the three transit time bands as the short-τ, mid-τ, and long-τ bands.

[34] Figure 11 shows the effect of [39]Ar on the inversions for the mass fraction in each transit time band as a function of the ideal mean age of the bottle (determined with [39]Ar). Of particular interest is the Pacific, where inferred mean age increases approximately monotonically with depth (Figure 7), mimicking 1d advection-diffusion. Comparison of the Pacific panel of Figure 11 for the uniform prior with Figure 5 shows that the Pacific profiles and the idealized 1d model have broadly similar behavior in how the changes in water mass fractions depend on ideal mean age. For the case of the uniform prior, this behavior may again be attributed to the fact that [39]Ar gives the ME functional form of the TTD freedom to build a mode away from the CFC limit at ~70a. With the AD prior a clear pattern for the Pacific is not apparent, except that the largest changes occur for the

Figure 9. The fraction Γ/Δ for the inversions with the AD prior and ^{39}Ar. Error bars were estimated as discussed in Appendix B. Symbol shapes and colors identify the location of the ^{39}Ar measurements as in Figure 1.

bottles with the oldest ideal mean age, which contain generally more water in the long-τ band with ^{39}Ar than without. The Atlantic bottles are generally younger and hence there is little change in the long-τ band, which contains little water. When ^{39}Ar is included, the dominant effect on the Atlantic bottles is an increase in the mass fraction in the mid-τ band at the expense of the mass in the short-τ band, with less systematic behavior for the AD prior than for the uniform prior.

[35] Figure 12 quantifies the reduction in the entropic uncertainty of the mass fractions in each of the three transit time bands due to including ^{39}Ar as an extra constraint. The uncertainty reduction is simply defined as the ratio, R, of the quartile error bar without ^{39}Ar to the error bar with ^{39}Ar. For the uniform prior, including ^{39}Ar reduces the uncertainty ($R > 1$) for essentially all bottles. The small amount of scatter below $R = 1$ is likely an artifact of approximating the entropic pdf of f_1 by fitting it to two points on either side of the ME value (a five-point fit). For the AD prior it is very interesting to note that while the uncertainty is reduced ($R > 1$) for most bottles, for some 18 bottles inclusion of ^{39}Ar turns out to increase the uncertainty ($R < 1$). We have closely examined our estimates of the entropic pdfs of f_1

to ensure that the effect is not merely an artifact of our five-point fit, although the approximation likely accounts for some of the points with R below unity by only a small amount ($\sim$0.05). We find that significant increases in uncertainty ($R < 1$) can occur with the AD prior when the inversion without ^{39}Ar gives a ME value of f_1 close to either extreme of $f_1 = 0$ or $f_1 = 1$, which is then shifted significantly away from its extreme when ^{39}Ar is included. We have yet to uncover the detailed mechanism by which a nonuniform prior can lead to uncertainty increases when an extra constraint is included, but we are able to reproduce the effect with the idealized 1d model of section 4 when the prior consists of an IG distribution with a prior mean age that is significantly larger (by a factor of $\sim$1.5) than that of the true underlying boundary propagator.

[36] The reductions in the uncertainty of the water mass fractions averaged over the bottles for which $R \geq 1$ are similar for the uniform and AD prior cases: approximately 50% for the short-τ, 20% for the mid-τ, and 30% for the long-τ band, with R exceeding a factor of two for about a dozen bottles. Including ^{39}Ar thus provides the greatest constraint on the short and long transit time water mass fractions. The dependence of the uncertainty reduction on
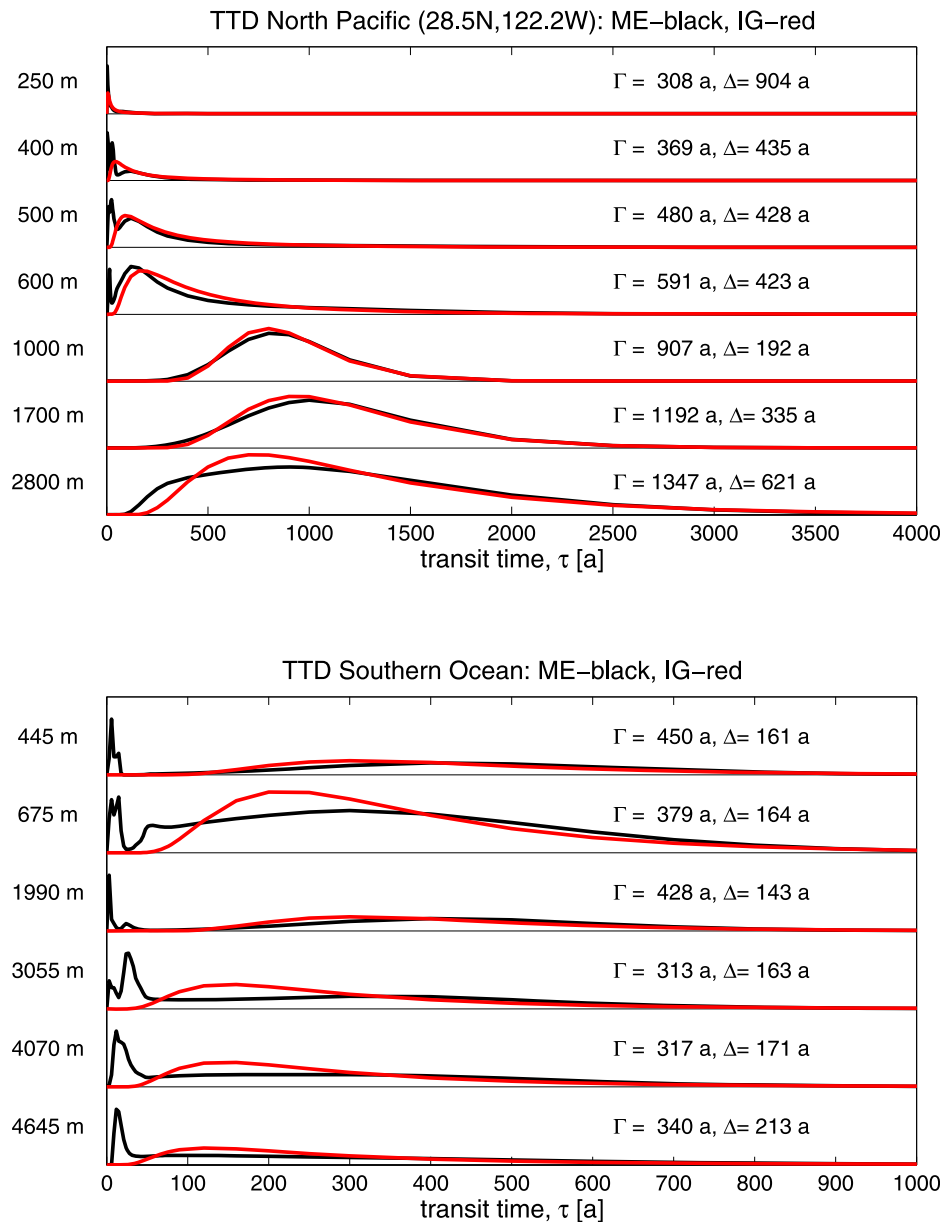
Figure 10. (top) The global TTDs for the Pacific profile at 28.5°N, 122.2°W and (bottom) for the Southern Ocean data. The black curves correspond to the ME solutions, while the red curves are inverse Gaussians of the same ideal mean age, Γ, and width, Δ, as indicated next to the curves. Every pair of ME TTD and corresponding inverse Gaussian has been normalized by the peak value of the ME TTD.

ideal mean age, Γ, shows a great deal of scatter, but generally most bottles with $\Gamma \gtrsim 700a$ show a significant reduction in uncertainty, while most bottles younger than that (largely from the Atlantic) have smaller uncertainty reductions.

[37] The uncertainty reduction for ideal mean age, Γ, that results from including ^{39}Ar as an extra constraint is evident in Figure 7, particularly for the Pacific and Southern Ocean locations. Detailed examination of the uncertainty reduction ratio showed that in the case of the AD prior about a dozen bottles, most in the Atlantic thermocline and abyss and four in the Pacific thermocline, again experience an increase in uncertainty when ^{39}Ar is included. Some of the effect may be due to our five-point approximation when the entropic

pdfs of Γ are highly skewed, but for most of these bottles the effect is likely similar to what was seen for the water mass fractions. Importantly, however, for most locations ^{39}Ar reduces the uncertainty in Γ with average reduction ratios of 1.3 in the Atlantic, 1.3 in the Pacific, and 2.0 in the Southern Ocean.

[38] Figure 13 examines the changes in the mass fraction in the short-τ band, f_1, when ^{39}Ar is included as an additional transient tracer. For nearly all bottles, and for both the uniform and AD priors, the short-τ fraction is substantially reduced except for the deep Pacific bottles that tend to be too old to contain much short-τ water. For the case of the uniform prior, the reduction in f_1 is consistent with the
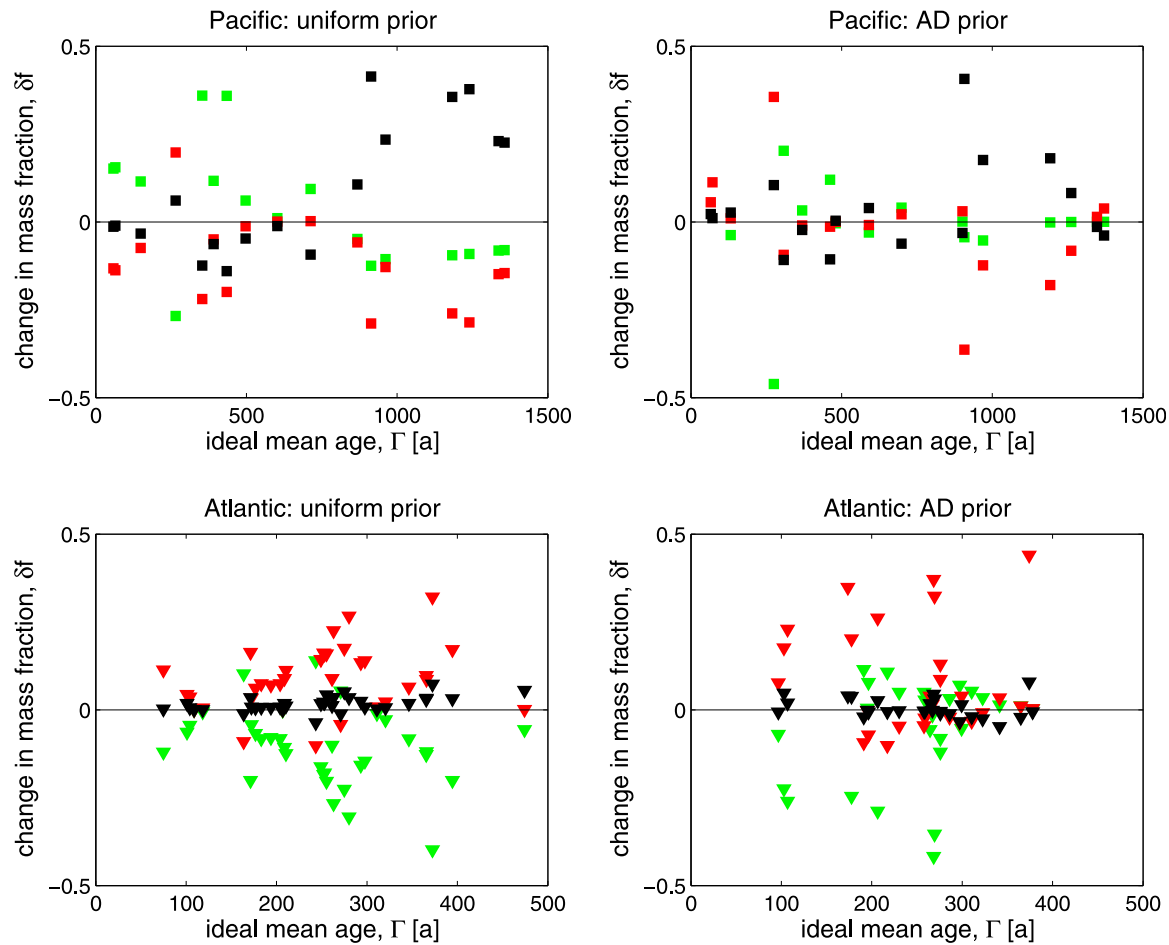
Figure 11. The change of the mass fraction, δf, (with [39]Ar minus no [39]Ar) in each of the three transit time bands considered (short-τ in green, mid-τ in red, long-τ in black) versus ideal mean age (determined with [39]Ar) for the Pacific and Atlantic bottles. Shown are the (left) uniform prior case and (right) AD prior case. Note the different age scales for the Pacific and Atlantic.

additional degree of freedom afforded by [39]Ar, which allows the TTD to have a mode beyond 70a, and hence less water with transit times within the CFC period. For the case of the AD prior with its nontrivial structure, there is no obvious mechanism that should lead to reduced f_1 values. The outlier point for the AD prior case that shows a large increase from $f_1 = 0.15$ to $f_1 = 0.92$ lies at 37.3°N, 45.4°W, and 3970 m depth in the North Atlantic. This point has similar behavior in the uniform prior case with an increase from $f_1 = 0.47$ to $f_1 = 0.80$, which does not show as prominently on the plot. An increase of f_1 as the result of [39]Ar as an extra constraint simply means that the observed [39]Ar concentration is larger than expected on the basis of the other tracer constraints.

[39] It is very interesting to note that the mass fractions obtained with [39]Ar are roughly the same regardless of whether we use the uniform or AD prior. This is emphasized in Figure 13 (bottom) by plotting the inversions for f_1 with the AD prior versus those using the uniform prior, both with [39]Ar. The scatter around the diagonal is much smaller than the changes in f_1 resulting from the inclusion of [39]Ar. While we expect that the choice of prior becomes secondary once enough data is used in the inversion, it is remarkable that

just four transient tracers (CFC-11, CFC-12, ^{14}C, and [39]Ar) already places the still highly underdetermined inversions in a regime of insensitivity to the choice of prior.

[40] The changes in the estimates of ideal mean age, Γ, that result from including [39]Ar in the ME inversions are quantified in Figure 14 for the uniform and AD prior cases. (Only bottles with $\Gamma \leq 500a$ are shown to make the changes more visible. For the older Pacific bottles, in the case of the AD prior, the changes in Γ are much smaller.) As expected from the reductions in the water mass fractions with $\tau < 105a$, for most bottles the ideal mean age is estimated to be older when [39]Ar is included. Note that this is not a statement about either the AD or uniform priors having a young bias. (In fact, the uniform prior has an old bias with a mean age of 10000a.) Instead, the inclusion of [39]Ar corrects a young bias in the ME TTDs as constrained by all the other tracers. The bottom plot of Figure 14 shows that for most locations the choice of prior is secondary for determining the ME value of Γ when [39]Ar is included. This insensitivity to the choice of prior is similar to that seen for f_1 in Figure 13 and is particularly striking in light of the fact that the ideal mean age of the uniform prior is 10000 a for all
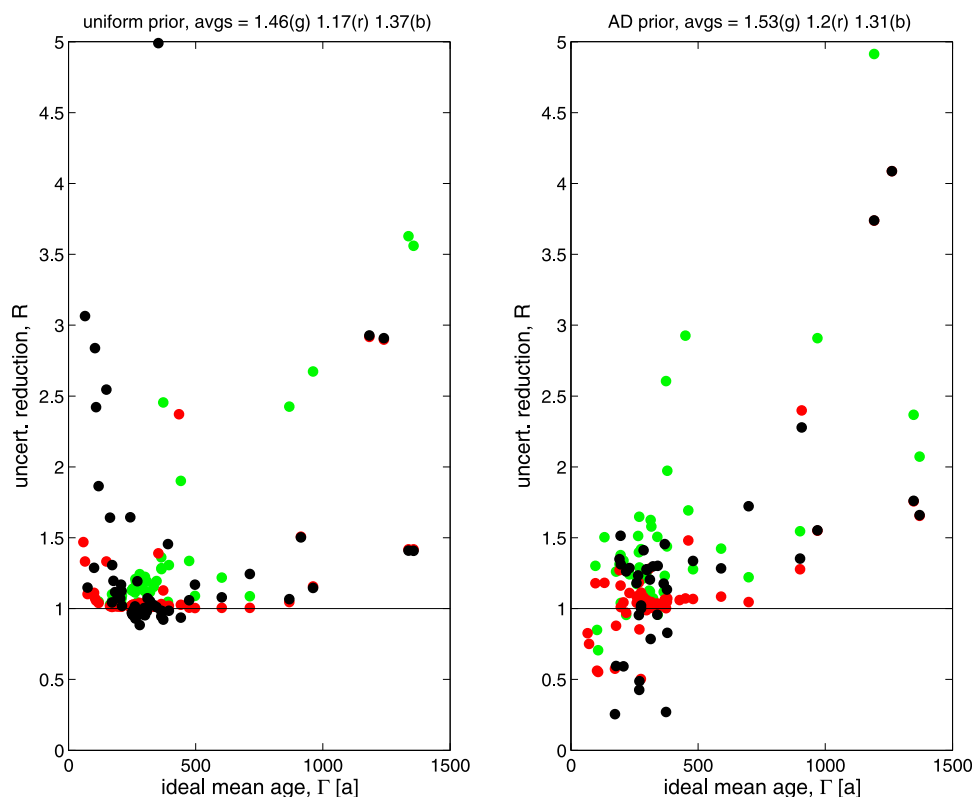
Figure 12. The reduction of the entropic uncertainty in the mass fraction in each transit time band (short-τ in green, mid-τ in red, long-τ in black) as a function of ideal mean age, Γ. The uncertainty reduction is defined as the ratio, R, of the size of the entropic quartile error bar without ^{39}Ar to the size of the quartile error bar when ^{39}Ar is included. The reduction R is plotted as function of the mean age of the bottle (determined with ^{39}Ar included) for the case of the (left) uniform prior and (right) AD prior, and the mean value of R for the bottles for which $R \geq 1$ is indicated in the title for each transit time band (g is short-τ, r is mid-τ, b is long-τ).

locations, while the AD prior has a more realistic distribution of ideal mean age [*Holzer et al.*, 2010].

6. Discussion

[41] In this paper we quantified the extent to which ^{39}Ar helps constrain specific diagnostic properties of the ocean's TTDs, namely ideal mean age, TTD width, and the water mass fraction in specified transit time bands. It is important to appreciate, however, that the value of any tracer constraint depends on the particular diagnostic property one is interested in. For example, we found that ^{39}Ar helped reduce the uncertainty in the water mass fractions with short and long transit times, but had much less effect on the uncertainties in the 105–550a transit time band even though this band brackets the ^{39}Ar decay timescale. The utility of a given transient tracer not only depends on its time dependence, but also critically on the spatial pattern of its surface boundary condition. Thus, ^{39}Ar with its nearly uniform boundary condition is expected to be of little use in constraining where water was last ventilated. Conversely, the spatial structure of a tracer's boundary condition has implications for estimating timescales. For example, ^{14}C with its very long decay timescale has a favorable temporal structure to constrain the ideal mean age, but its spatially inhomoge-

neous surface boundary condition is not well matched to the uniform boundary condition of the ideal mean age [*Holzer et al.*, 2010; *DeVries and Primeau*, 2010]. In contrast, ^{39}Ar has a uniform boundary condition, but its faster decay projects less well onto the linear dependence desired to constrain mean age. The utility of ^{39}Ar as a constraint will also depend on what other tracer constraints are available. In general, the incremental reduction in uncertainty with each additional constraint is expected to decrease as the total number of constraints increases. Finally, the impact of ^{39}Ar data on the maximum entropy inversion will depend on the choice of prior. For example, if the prior already encodes the information contained in ^{39}Ar, then ^{39}Ar would have no effect on the inversions. For the uniform and AD priors employed here, ^{39}Ar provided additional constraints in about equal measure.

[42] It is worth contrasting TTD estimates using the now popular parametric IG approach [e.g., *Waugh et al.*, 2003; *Huhn et al.*, 2008; *Tanhua et al.*, 2009; *DeVries and Primeau*, 2010] to the ME approach employed here. The parametric approach assumes that the TTD can be captured to a good approximation by an IG distribution that is completely specified by two parameters: its mean and variance, or equivalently, Γ and Δ. With three transient tracer constraints, IG deconvolutions are thus formally overdetermined and the residual from a best fit could be used to
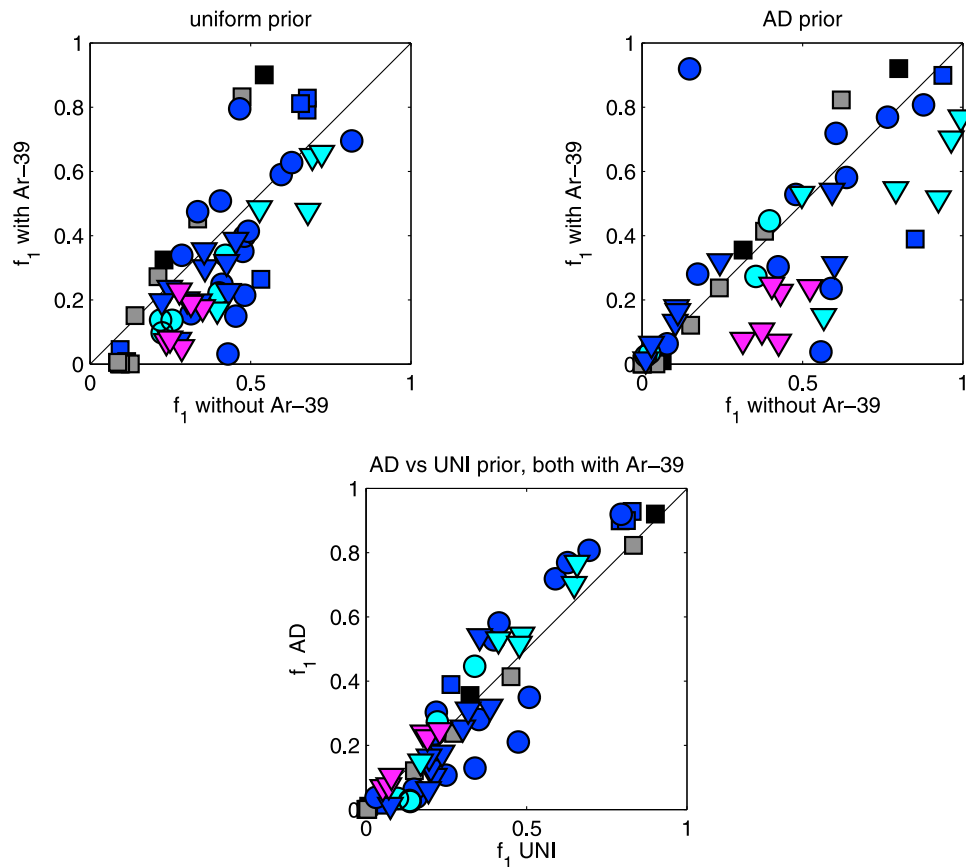
Figure 13. (top) The two plots show the mass fraction f_1 of water with transit time $\tau \in [0, 105]$a, as computed with ^{39}Ar versus the same quantity computed without ^{39}Ar for the cases of uniform and AD prior, as indicated. (bottom) The plot shows f_1 computed with the AD prior versus f_1 computed with the uniform prior, both with ^{39}Ar. Symbol shapes and colors identify the location of the ^{39}Ar measurements as in Figure 1.

estimate an uncertainty in the IG parameters. However, this apparent overdeterminedness is artificial for several reasons. First, the unimodal IG functional form cannot properly account for the mixing of different end-members, information that is encoded in tracers such as radiocarbon that have large spatial variations in their surface concentration. Indeed, the most probable shape of the TTDs as estimated by the ME deconvolutions is typically multimodal and not everywhere well approximated by an IG. While a superposition of multiple IG functions could in principle take into account multiple end-members, the number of parameters that would need to be estimated from the data quickly exceeds the number of available tracer constraints. Second, the deconvolution is fundamentally highly underdetermined. Even if the tracer boundary conditions were spatially uniform, each radioactive tracer with decay constant λ can be thought of as constraining only a single point of the Laplace transform of the TTD, $\widetilde{\mathcal{G}}(s) = \int_0^\infty \exp(-s\tau)\mathcal{G}(\tau)d\tau$, at $s = \lambda$, underscoring the fact that the available tracer constraints leave the problem highly underdetermined. A key advantage of the ME deconvolutions is that it allowed us to estimate the uncertainty associated with this underdeterminedness. Legislating the TTD to be of IG form artificially suppresses the true uncertainty of the deconvolutions except for the

case where there is certain prior knowledge that the TTD should closely follow the IG form. In this regard parametric inversions of tracer data for the TTD are analogous to the OMP method for determining water mass fractions [e.g., *Tomczak*, 1981; *Tomczak and Large*, 1989] where the number of possible end-members is fixed by hand, thereby artificially suppressing the underdetermined nature of the data inversions [*Holzer et al.*, 2010].

7. Conclusions

[43] The focus of this paper has been on the transit time information provided by passive oceanographic tracers when ^{39}Ar measurements are used to bridge the gap between the short-timescale CFCs and the long-timescale radiocarbon. To this end, we analyzed the transient tracers CFC-11, CFC-12, ^{39}Ar, and ^{14}C, as well as the climatologically cyclostationary scalars θ, S, and PO$_4$*, which contain additional information on where a fluid element was last in the mixed layer. The vastly underdetermined problem of deconvolving the tracer concentrations at point $\mathbf{r}$ for the mass fractions $\mathcal{P}(s, \tau|\mathbf{r})$ that had a transit time τ from surface grid box s to $\mathbf{r}$, was regularized using a maximum entropy method. Because our focus is on the effect of ^{39}Ar,
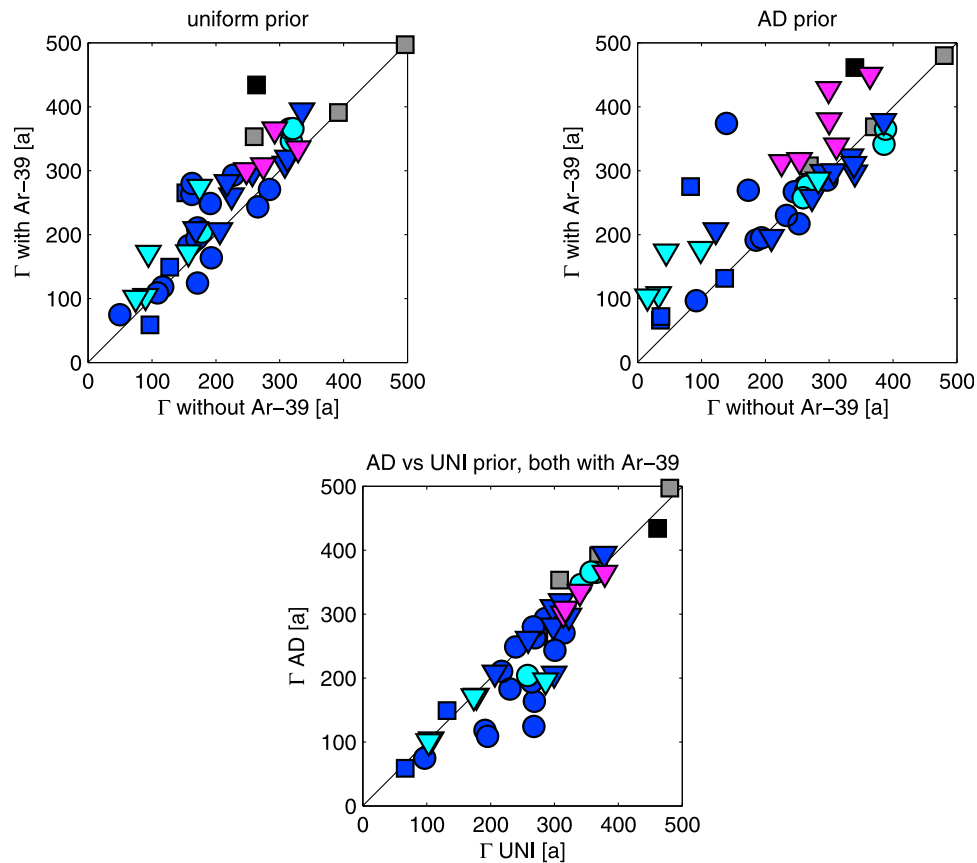
Figure 14. Ideal mean age, Γ, with [39]Ar versus Γ without [39]Ar as determined by the ME deconvolutions. The bottom plot shows Γ computed with the AD prior versus Γ computed with the uniform prior, both with [39]Ar. Symbol shapes and colors identify the location of the [39]Ar measurements as in Figure 1.

which contains virtually no surface origin information, we limited analysis to the global integral of $\mathcal{P}$ over surface origin, otherwise also known as the TTD, its ideal mean age, Γ, and width, Δ, and the mass fractions in specified transit time bands. The uncertainties of these quantities were estimated from their entropic probability distributions, neglecting uncertainties associated with the variability of the tracer concentrations [*Holzer et al.*, 2010]. Our conclusions are as follows:

[44] 1. Our ME deconvolutions revealed a spatial structure in the ideal mean age Γ and in the water mass fraction f_1 with $\tau \lesssim 105$ a that is consistent with the known distributions of NADW, AAIW, and AABW in the Atlantic and with the simpler water mass structure of the Pacific. In addition to this qualitative consistency, our deconvolutions allowed us to obtain quantitative estimates of Γ, the TTD width Δ, and f_1, together with estimates of their entropic uncertainties (Figures 6, 7, and 8). Inclusion of [39]Ar led to reduced values of f_1 for the majority of the locations analyzed with mean ages that were correspondingly longer by about a century (Figures 13 and 14).

[45] 2. For the Southern Ocean, a region of vigorous overturning where deep waters are both formed and upwelled, our ME deconvolutions produced TTDs with little depth dependence compared to other basins. At all depths, our inferred TTDs for the Southern Ocean had a mode at short

transit times indicating the presence of newly ventilated waters and a long slowly decaying tail indicating the upwelling of old waters back to the surface.

[46] 3. Having [39]Ar available as an additional transient tracer tends to reduce the entropic uncertainty in our estimates of ideal mean age, TTD width, and water mass fractions. For the water mass fractions the reductions range on average from ~20% to ~50% depending on the transit time band considered, and for ideal mean age the uncertainty is halved in the Southern Ocean with reductions of ~30% elsewhere. With the uniform prior, including [39]Ar either reduced or left unchanged the size of the entropic error bars at all locations. With the nonuniform AD prior, including [39]Ar reduced the uncertainty for most locations, but for some bottles the uncertainty actually increased. Increases in uncertainty are typically accompanied by a substantial shift in the ME value of the diagnostic. Thus, while ME deconvolutions are guaranteed to uncover the true boundary propagator and its moments in the limit of an infinite number of tracer constraints, the reduction of entropic uncertainty in the approach to this limit can be nonmonotonic with a nonuniform prior.

[47] 4. The ME deconvolutions highlight the fact that TTDs generally do not have a simple unimodal IG form that is determined by only two parameters. Our ME deconvolutions do not fix the functional form of the TTD at the outset,

which is reflected in substantial entropic uncertainties for mean age, Γ, and even greater uncertainties for the TTD width, Δ. The ratio Γ/Δ is also not as narrowly constrained as parametric inversions suggest [*Waugh et al.*, 2003; *Hall et al.*, 2004]. The implication is that IG-based estimates of Γ and Δ are insufficient to characterize transport from the surface because they ignore the large uncertainty associated with the underdetermined nature of the inversion.

[48] 5. In the deep Pacific were CFCs have not yet penetrated, using both [39]Ar and ^{14}C allows determination of a TTD with a realistic shape even when a uniform prior without any transit time information is used. With only ^{14}C and a uniform prior the ME solution would give a TTD with an unrealistic shape of a monotonically decreasing function with a nonzero value at $\tau = 0$.

[49] 6. The additional transient tracer [39]Ar gives the maximum entropy solution for the boundary propagator additional freedom. In the case of the uniform prior, having only CFCs and radiocarbon unrealistically constrains the mode of the propagator to lie within the CFC period ($\sim$70a) regardless of the tracer concentrations. Including [39]Ar relaxes this constraint so that even with a uniform prior the deconvolved TTD is free to place its mode at any transit time.

[50] 7. The Pacific profiles come closest to approximating the behavior of simple 1d advection-diffusion, particularly below the thermocline where the TTDs become unimodal with a shape that is at least roughly approximated by an IG functional form. In the case of the ME inversions with the uniform prior for the Pacific data, the effect of including [39]Ar on the estimated water mass fractions in a given transit time interval is similar to the effect seen for a simple 1d model with synthetic data generated by an IG TTD.

[51] 8. Remarkably, [39]Ar in combination with the other six tracers already provides a sufficient number of constraints to make the inversions relatively insensitive to the choice of prior. Deconvolutions using either the uniform or AD prior give similar results both in the case of the mass fraction of water with transit times less than $\sim$100a and in the case of ideal mean age.

[52] Using [39]Ar as an additional transient tracer led to substantial changes in our ME estimates of ideal mean age, TTD width, and water mass fractions, while at the same time reducing their entropic uncertainties. There is no question that an effort to produce a globally gridded [39]Ar data set would greatly help reduce the uncertainty in our knowledge of oceanic transport and ventilation, which in turn would greatly benefit rigorous estimates of the ocean's ability to take up and sequester anthropogenic carbon.

Appendix A: Numerical Details

[53] For the inversions with the oceanographic data (as opposed to the 1d model), transit time was resolved as follows: $\tau \in [0, 3, 6,\ldots, 75, 80, 90, 120, 160, 200, 250, 300, 400, \ldots, 1000, 1200, 1500, 2000, \ldots, 4000, 5000, 7000, 9000, 11000, 15000, 20000]$a. Integrations over transit time bands were performed by zeroing $\tau \in [120, 20000]$ a for band one, $\tau \in [0, 90] \cup [600, 20000]$ a for band two, and $\tau \in [600, 20000]$ a for band three, followed by trapezoidal integration over all transit times. Thus, for example, the edge of the youngest transit time band has a linear taper

from 90 to 120a. The approximate boundaries between the transit time bands therefore lie at 105 and 550a.

Appendix B: Uncertainty Propagation

[54] While entropic uncertainties in moments of the TTD's can straightforwardly be computed, uncertainties in nonlinear functions of these moments are more difficult to compute. Here we approximate the error in the TTD width $\Delta \equiv \sqrt{(m_2 - \Gamma^2)/2}$ by making the ansatz that the uncertainties in the mean age (first moment) and in the second moment $m_2 \equiv \int_0^\infty \tau^2 \mathcal{G}(\tau)d\tau$ can be treated as statistically independent for the purpose of estimating the error in Δ. Given uncertainties $\delta\Gamma$ and δm_2, we therefore approximate the error in Δ as $\delta\Delta = \sqrt{(\partial\Delta/\partial\Gamma)^2(\delta\Gamma)^2 + (\partial\Delta/\partial m_2)^2(\delta m_2)^2}$. Asymmetric error bounds for Δ were calculated by separately using the right and left entropic error bars calculated for Γ and m_2.

[55] The uncertainty bounds on the ratio Γ/Δ was estimated roughly as $[\Gamma_{min}/\Delta_{max}, \Gamma_{max}/\Delta_{min}]$, where $[\Gamma_{min}, \Gamma_{max}]$ are the probability bounds on the entropic uncertainty of the mean age (the left and right limits of our entropic error bars), and $[\Delta_{min}, \Delta_{max}]$ are the uncertainty bounds calculated as described in the previous paragraph.

References

Antonov, J. I., R. A. Locarnini, T. P. Boyer, A. V. Mishonov, and H. E. Garcia (2006), *World Ocean Atlas* 2005, vol. 2, *Salinity*, *NOAA Atlas NESDIS*, vol. 62, edited by S. Levitus, 182 pp., NOAA, Silver Spring, Md.

Broecker, W., and T.-H. Peng (2000), Comparison of [39]Ar and ^{14}C ages for waters in the deep ocean, *Nucl. Instrum. Methods Phys. Res., Sect. B*, *172*, 473–478.

Broecker, W. S., et al. (1998), How much deep water is formed in the Southern Ocean?, *J. Geophys. Res.*, *103*, 15,833–15,843, doi:10.1029/98JC00248.

DeVries, T., and F. Primeau (2010), An improved method for estimating water mass ventilation age from radiocarbon measurements, *Earth Planet. Sci. Lett.*, *295*, 367–378.

Foster, T. D., and E. C. Carmack (1976), Frontal zone mixing and Antarctic Bottom Water formation in the southern Weddell Sea, *Deep Sea Res. Oceanogr. Abstr.*, *23*, 301–317.

Gaelens, M., M. Loiselet, G. Ryckewaert, R. C. Pardo, R. H. Scott, R. Vondrasek, P. Collon, and W. Kutchera (2005), Oceans circulation and electron cyclotron resonance sources: Measurement of the Ar-39 isotopic ratio in seawater, *Rev. Sci. Instrum.*, *75*, 1916–1918.

Garcia, H. E., R. A. Locarnini, T. P. Boyer, and J. I. Antonov (2006a), *World Ocean Atlas* 2005, vol. 3, *Dissolved Oxygen, Apparent Oxygen Utilization, and Oxygen Saturation*, *NOAA Atlas NESDIS*, vol. 63, edited by S. Levitus, 342 pp., NOAA, Silver Spring, Md.

Garcia, H. E., R. A. Locarnini, T. P. Boyer, and J. I. Antonov (2006b), *World Ocean Atlas* 2005, vol. 4, *Nutrients (Phosphate, Nitrate, and Silicate)*, *NOAA Atlas NESDIS*, vol. 64, edited by S. Levitus, 396 pp., NOAA, Silver Spring, Md.

Gehrie, E., D. Archer, S. Emerson, C. Stump, and C. Henning (2006), Subsurface ocean argon disequilibrium reveals the equatorial Pacific shadow zone, *Geophys. Res. Lett.*, *33*, L18608, doi:10.1029/2006GL026935.

Gull, S. F., and G. J. Daniell (1978), Image reconstruction from incomplete and noisy data, *Nature*, *272*, 686–690.

Hall, M. M., T. M. Joyce, R. S. Pickart, W. M. Smethie, and D. J. Torres (2004), Zonal circulation across 52°W in the North Atlantic, *J. Geophys. Res.*, *109*, C11008, doi:10.1029/2003JC002103.

Hall, T. M., and R. A. Plumb (1994), Age as a diagnostic of stratospheric transport, *J. Geophys. Res.*, *99*, 1059–1070, doi:10.1029/93JD03192.

Holzer, M., and T. M. Hall (2000), Transit time and tracer-age distributions in geophysical flows, *J. Atmos. Sci.*, *57*, 3539–3558.

Holzer, M., F. W. Primeau, W. M. Smethie, and S. Khatiwala (2010), Where and how long ago was water in the western North Atlantic ventilated? Maximum entropy inversions of bottle data from WOCE line A20, *J. Geophys. Res.*, *115*, C07005, doi:10.1029/2009JC005750.

Huhn, O., W. Roether, and R. Steinfeldt (2008), Age spectra in North Atlantic Deep Water along the South American continental slope, 10°–30°S, based on tracer observations, *Deep Sea Res., Part I*, *55*, 1252–1276.

Jaynes, E. T. (1957), Information theory and statistical mechanics, *Phys. Rev.*, *106*, 620–630.

Key, R. M., A. Kozyr, C. L. Sabine, K. Lee, R. Wanninkhof, J. L. Bullister, R. A. Feely, F. J. Millero, C. Mordy, and T.-H. Peng (2004), A global ocean carbon climatology: Results from Global Data Analysis Project (GLODAP), *Global Biogeochem. Cycles*, *18*, GB4031, doi:10.1029/2004GB002247.

Locarnini, R. A., A. V. Mishonov, J. I. Antonov, T. P. Boyer, and H. E. Garcia (2006), *World Ocean Atlas 2005*, vol. 1, *Temperature*, *NOAA Atlas NESDIS*, vol. 61, edited by S. Levitus, 182 pp., NOAA, Silver Spring, Md.

Loosli, H. H. (1983), A dating method with ^{39}Ar, *Earth Planet. Sci. Lett.*, *63*, 51–62.

Loosli, H. H. (1989), ^{39}Ar: A tool to investigate ocean water circulation and mixing, in *Handbook of Environmental Isotope Chemistry*, vol. 3, *The Marine Environment*, edited by P. Fritz and C. Fontes, pp. 385–392, Elsevier, New York.

Luyten, J. R., J. Pedlosky, and H. Stommel (1983), The ventilated thermocline, *J. Phys. Oceanog.*, *13*, 292–309.

Maier-Reimer, E. (1993), Geochemical cycles in an ocean general circulation model. Preindustrial tracer distributions, *Global Biogeochem. Cycles*, *7*, 645–677, doi:10.1029/93GB01355.

Orsi, A. H., G. C. Johnson, and J. L. Bullister (1999), Circulation, mixing, and production of Antarctic Bottom Water, *Prog. Oceanogr.*, *43*, 55–109.

Press, W., S. Teukolsky, W. Vetterling, and B. Flannery (2007), *The Art of Scientific Computing*, 3rd ed., Cambridge Univ. Press, Cambridge, U. K.

Rodriguez, J. (1993), Beitrage zur Verteilung von ^{39}Ar im Atlantik, Ph.D. thesis, Inauguraldissertation der Philosophisch-naturwissenschaftlichen Fakultät der Univ. ät Bern zur Erlangung der Doktorwurde, Bern, Switzerland.

Sabine, C. L., R. M. Key, A. Kozyr, R. A. Feely, R. Wanninkhof, F. J. Millero, T.-H. Peng, J. L. Bullister, and K. Lee (2005), Global Ocean Data Analysis Project: Results and data, ORNL/CDIAC-145 NDP-083, Carbon Dioxide Inf. Anal. Cent., Oak Ridge Natl. Lab., Oak Ridge, Tenn.

Schlitzer, R., W. Roether, U. Weidmann, P. Kalt, and H. H. Loosli (1985), A meridional ^{14}C and ^{39}Ar section in Northeast Atlantic Deep Water, *J. Geophys. Res.*, *90*, 6945–6952.

Shannon, C. E. (1951), Prediction and entropy of printed English, *Bell Syst. Tech. J.*, *30*, 50–64.

Skilling, J., and S. F. Gull (1991), Bayesian maximum entropy image reconstruction, in *Spatial Statistics and Imaging: Papers from the Research Conference on Image Analysis and Spatial Statistics held at Bowdoin College, Brunswick, Maine, Summer 1988*, edited by A. Possolo, pp. 341–367, Instit. of Math. Stat., Hayward, Calif.

Tanhua, T., E. P. Jones, E. Jeansson, S. Jutterström, W. M. Smethie, D. W. R. Wallace, and L. G. Anderson (2009), Ventilation of the Arctic Ocean: Mean ages and inventories of anthropogenic CO_2 and CFC-11, *J. Geophys. Res.*, *114*, C01002, doi:10.1029/2008JC004868.

Tomczak, M. (1981), A multiparameter extension of temperature/salinity diagram techniques for the analysis of non-isopycnal mixing, *Prog. Oceanogr.*, *10*, 147–171.

Tomczak, M., and D. G. Large (1989), Optimum multiparameter analysis of mixing in the thermocline of the eastern Indian Ocean, *J. Geophys. Res.*, *94*, 16,141–16,149.

Walker, S. J., R. F. Weiss, and P. K. Salameh (2000), Reconstructed histories of the annual mean atmospheric mole fractions for the halocarbons CFC-11, CFC-12, CFC-113 and carbon tetrachloride, *J. Geophys. Res.*, *105*, 14,285–14,296, doi:10.1029/1999JC900273.

Waugh, D. W., T. M. Hall, and T. W. N. Haine (2003), Relationships among tracer ages, *J. Geophys. Res.*, *108*(C5), 3138, doi:10.1029/2002JC001325.

Waugh, D. W., T. W. N. Haine, and T. M. Hall (2004), Transport times and anthropogenic carbon in the subpolar North Atlantic Ocean, *Deep Sea Res., Part I*, *51*, 1475–1491.

Waugh, D. W., T. M. Hall, B. I. McNeil, R. Key, and R. J. Matear (2006), Anthropogenic CO_2 in the oceans estimated using transit time distributions, *Tellus Ser. B*, *58*, 376–389.

Welte, J., F. Ritterbusch, I. Steinke, M. Henrich, W. Aeschbach-Hertig, and M. K. Oberthaler (2010), Towards the realization of atom trap trace analysis for ^{39}Ar, *N. J. Phys.*, *12*, 065031, doi:10.1088/1367-2630/12/6/065031.

M. Holzer, Department of Applied Mathematics, School of Mathematics and Statistics, University of New South Wales, Sydney, NSW 2052, Australia. (mholzer@unsw.edu.au)

F. W. Primeau, Department of Earth System Science, University of California, 3216 Croul Hall, Irvine, CA 92697-3100, USA. (fprimeau@uci.edu)